TITLE

Large haploblocks underlie rapid adaptation in an invasive weed

AUTHORS

Paul Battlay[1], Jonathan Wilson[1], Vanessa C. Bieker[2], Christopher Lee[1], Diana Prapas[1], Bent Petersen[3,4], Sam Craig[1], Lotte van Boheemen[1], Romain Scalone[5,6], Nissanka P. de Silva[1], Amit Sharma[7], Bojan Konstantinović[8], Kristin A. Nurkowski[1,9], Loren H. Rieseberg[9], Tim Connallon[1], Michael D. Martin[2], Kathryn A. Hodgins[1]*

These authors contributed equally: Paul Battlay, Jonathan Wilson

These authors jointly supervised this work: Kathryn A. Hodgins, Michael D. Martin

[1] School of Biological Sciences, Monash University, Melbourne, Victoria, Australia

[2] Department of Natural History, NTNU University Museum, Norwegian University of Science and Technology (NTNU), Trondheim, Norway

[3] Center for Evolutionary Hologenomics, GLOBE Institute, University of Copenhagen, Denmark

[4] Centre of Excellence for Omics-Driven Computational Biodiscovery (COMBio), AIMST University, 08100 Kedah, Malaysia

[5] Department of Crop Production Ecology, Uppsala Ecology Center, Swedish University of Agricultural Sciences, Uppsala, Sweden.

[6] Department of Grapevine Breeding, Hochschule Geisenheim University, Geisenheim, Germany.

[7] Cell, Molecular Biology and Genomics Group, Department of Biology, Norwegian University of Science and Technology (NTNU), Trondheim, Norway

[8] Department of Environmental and Plant Protection, University of Novi Sad, Novi Sad, Serbia

[9] Department of Botany and Biodiversity Research Centre, University of British Columbia, Vancouver, Canada

ABSTRACT

Adaptation is the central feature and leading explanation for the evolutionary diversification of life. Adaptation is also notoriously difficult to study in nature, owing to its complexity and logistically prohibitive timescale. We leverage extensive contemporary and historical collections of *Ambrosia artemisiifolia*—an aggressively invasive weed and primary cause of pollen-induced hayfever—to track the phenotypic and genetic causes of recent local adaptation across its native and invasive ranges in North America and Europe, respectively. Large haploblocks—indicative of chromosomal inversions—contain a disproportionate share (26%) of genomic regions conferring parallel adaptation to local climates between ranges, are associated with rapidly adapting traits, and exhibit dramatic frequency shifts over space and time. These results highlight the importance of large-effect standing variants in rapid adaptation, which have been critical to *A. artemisiifolia*'s global spread across vast climatic gradients.

INTRODUCTION

Adaptation can be rapid, yet changes in the traits and genes that underlie adaptation are difficult to observe in real time because speed is relative: that which is fast in evolutionary terms is slow from the human perspective. Thus, while we know that adaptation is central to evolutionary diversification, species persistence and invasiveness, the genetic and phenotypic dynamics of adaptation are difficult to document outside of the laboratory.

Invasive species are powerful systems for characterizing adaptation in nature, owing to several features that make them unique. In particular, biological invasions coincide with exceptionally rapid evolution[1–3], observable over human lifespans, as invasive populations can encounter drastically different environmental conditions from those of their source populations. Many invasions are, moreover, documented in large, geo-referenced herbarium collections, which can be phenotyped and sequenced to identify and track adaptive evolutionary changes through time—feats that are rarely achieved in natural populations. Invasive species frequently inhabit broad and climatically diverse ranges, which favours the evolution of adaptations to local environmental conditions[2,3], along with evolved tolerance of environmental extremes, which may be conducive to invasiveness[4]. Because they often occupy geographically broad native and invasive ranges, invasive species allow for tests of the predictability of evolution—a major puzzle in biology—as local adaptation across native and invasive ranges may favour either parallel or unique genetic solutions to shared environmental challenges. However, despite the promise of historical records and other features of invasive species that make them tractable systems for capturing adaptation in action, this treasure trove of data has not been fully utilized to elucidate the genetic basis of local adaptation during recent range expansions.

Ambrosia artemisiifolia, an annual weed native to North America, has mounted successful invasions on all continents except Antarctica[5]. The species thrives in disturbed habitats and has experienced extensive range shifts, historically documented in pollen records and herbarium collections. It also produces highly allergenic pollen, which is the chief cause of seasonal allergic rhinitis and asthma in the United States[6]. In Europe alone, approximately 13.5 million people suffer from *Ambrosia*-induced allergies, costing ~7.4 billion euros annually[7]. Continued invasion and climate change are predicted to more than double sensitization to *Ambrosia* pollen[8], further magnifying the health burden of this pest. Pollen monitoring has demonstrated that climate change has already significantly lengthened the ragweed pollen season, particularly at high latitudes[9]. Consequently, there is considerable incentive to understand the factors that

contribute to *Ambrosia* pollen production, including the species' invasive spread, the timing of pollen production, plant size, and fecundity.

Ambrosia artemisiifolia populations are characterized by strong local adaptation and high gene flow between populations[10,11]. In Europe, invasive populations have been established through multiple genetically diverse introductions from North America over the last ~160 years[11–13]. Remarkably, latitudinal clines observed for multiple traits in the native range, including flowering time and size, have re-evolved in Europe and Australia[14], suggesting rapid local adaptation following invasion. Moreover, this trait-level parallelism is echoed in signals of parallelism at the genetic level[10].

As biological invasions continue to increase worldwide[15] and the effects of anthropogenic climate change intensify, understanding the genetic architecture of adaptation to sudden environmental shifts—a classical question in evolutionary research—becomes ever more important. While long-standing theory suggests that evolution in response to incremental environmental change should proceed through mutations of infinitesimally small[16] or moderate[17] effect, large-effect mutations are predicted to be useful in bridging extreme, sudden environmental shifts[18]. Moreover, alleles of large effect will, in cases of local adaptation, be better able to persist in the face of the swamping effects of gene flow[19]. Large-effect mutations are also more likely to produce patterns of evolutionary repeatability, or genetic parallelism, between species' ranges[20], particularly if adaptive responses make use of standing genetic variation (as would be expected during a bout of rapid adaptation), rather than *de novo* mutations[21]. These features of large-effect mutations may, however, be achieved by groups of mutations in tight genetic linkage[19], including mutations captured by chromosomal inversions[22]. There is substantial empirical evidence for the involvement of inversions in local adaptation[23]. For example, *Drosophila melanogaster*'s *In(3R)Payne* inversion shows parallel environmental associations across multiple continents[24], and several plant inversions have been identified as contributing to local adaptation and ecotype divergence[25,26]. Theory also predicts that inversions can drive range expansions[27], though their actual contributions to biological invasions are not well-understood.

Here we develop a chromosome-level phased diploid reference assembly, and examine genome-wide variation in over 600 modern and historic *A. artemisiifolia* samples from throughout North America and Europe[11]. Using this data of unparalleled spatial and temporal

resolution, we first identified regions of the genome experiencing climate-mediated selection in the native North American and introduced European ranges leveraging landscape genomic approaches and genome-wide association studies of adapting traits such as flowering time. Second, motivated by evidence that European and North American populations show similar trait clines with respect to climate[14], we examined the extent of between-range parallelism at the genetic level. Although adaptive traits such as flowering time and size are polygenic, we expected to see substantial levels of parallelism if large and moderate effect standing variants were contributing to adaptive divergence. Third, we determined if these same regions show temporal signatures of selection in Europe, which would be expected if some invading populations were initially maladapted to their local climates. We coupled this temporal genomic analysis with a temporal analysis of phenological trait changes in European herbarium samples to further support our findings of genomic signatures of selection on flower time genes. Finally, we identified haplotype blocks with multiple features consistent with inversions, in genomic regions enriched for signatures of parallel adaptation. Four of these colocalize with inversions identified in our diploid assembly, confirming their identity as inversions. To determine if these haploblocks were contributing to rapid local adaptation in Europe, we assessed spatial and temporal changes in their frequency as well as their associations with adaptive traits.

RESULTS

Reference genome assembly

We assembled a chromosome-level phased diploid *Ambrosia artemisiifolia* reference genome (fig. 1; fig. S1) from a heterozygous, diploid individual collected from Novi Sad, Serbia. After scaffolding with HiRise[28], our final assembly consisted of two haploid assemblies with genome sizes of 1.11 and 1.07Gbp (flow cytometry estimates of genome size range from 1.13-1.16Gbp[29,30]), with 94.3 and 96.5% of each respective genome assembled into 18 large scaffolds (table S1; table S2), consistent with the 18 chromosomes of *A. artemisiifolia.* Complete copies of all 255 Benchmarking Universal Single-Copy Orthologs (BUSCO[31]) genes were identified on the 18 chromosomes of each haploid assembly, with 183 (71.8%) single-copy and 72 (28.2%) duplicated (fig. 1C; table S1). These high numbers of duplicated BUSCO genes likely reflect the whole-genome duplications experienced in the Asteraceae, including a recent one shared by *Helianthus* (sunflower) species at the base of the tribe[32,33]. This species also retained a large number of duplicated BUSCO genes[33]. A large fraction of the genome consisted of repetitive sequence (67%; table S3). Retroelements were the largest class (39.5%), with long terminal repeats, particularly Gypsy (7.87 %) and Copia (18.98 %), being the most prevalent. MAKER[34] identified 36,826 gene models with strong protein or transcript support, with average coding lengths of 3kbp and 5.75 exons per gene (fig 1A; table S4).

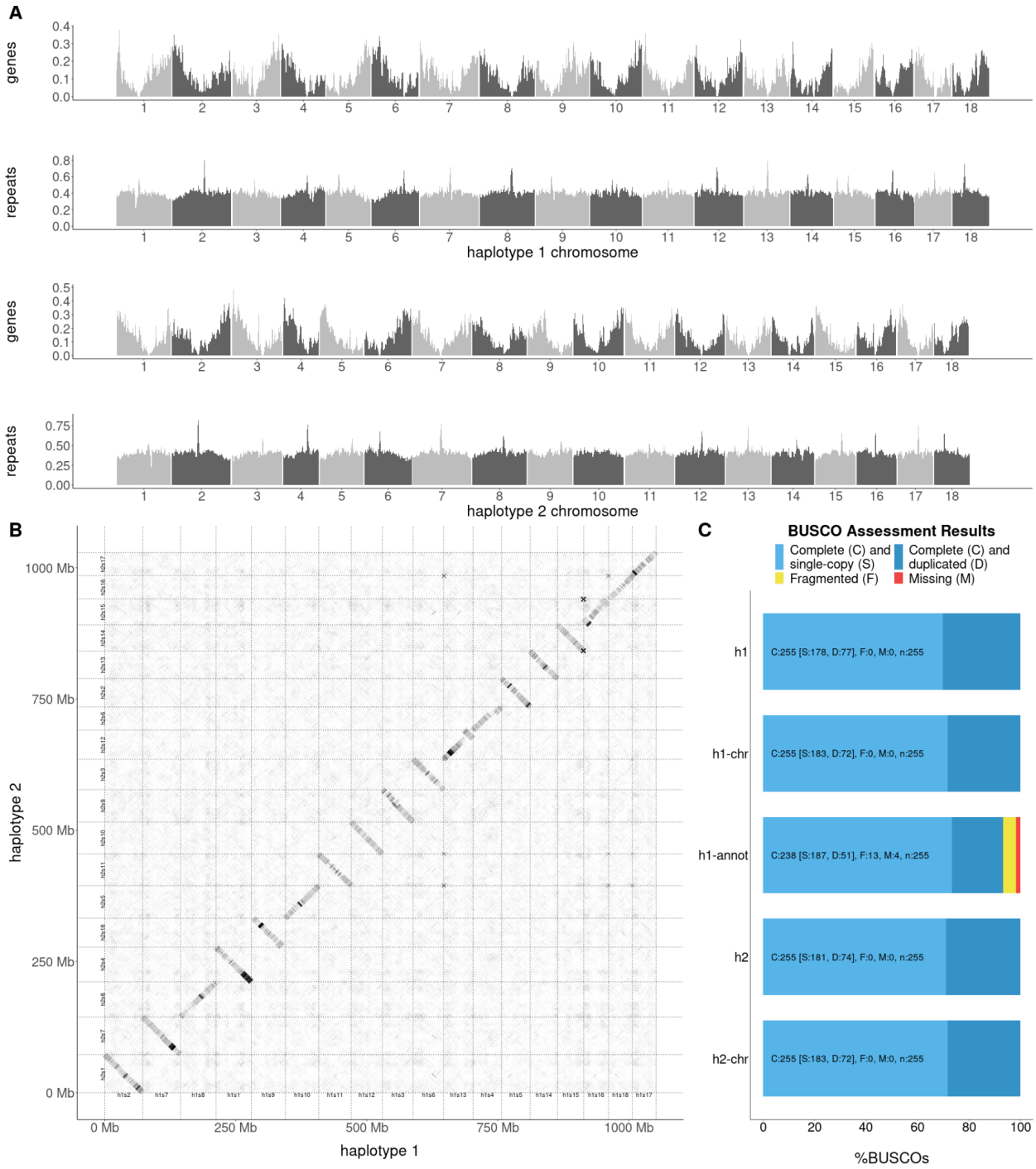

Figure 1. A phased diploid genome assembly of *Ambrosia artemisiifolia.* A. The distribution of gene and repeat density in 1Mbp windows across the 18 chromosomes of each haplotype. **B.** Alignments of the 18 chromosomes of each haplotype. **C.** Benchmarking Universal Single-Copy Orthologs (BUSCO) results for each haplotype assembly, each chromosome-only assembly, and the gene annotations for haplotype 1 using the *eukaryota odb10* gene set.

149 **Genome-wide association studies**

150 Genome-wide association studies (GWAS) using 121 modern samples across North American
151 (*n* = 43) and European (*n* = 78; table S5) ranges identified significant associations with 16 of 30
152 phenotypes, many of which are putatively adaptive, previously measured by van Boheemen,
153 Atwater and Hodgins[14] (fig. S2; table S6). All phenotypes yielded associations within at least
154 one predicted gene, including an association between three flowering time phenotypes and a
155 nonsynonymous SNP in the *A. artemisiifolia* homologue of *A. thaliana* flowering-time pathway
156 gene *early flowering 3* (*ELF3*)[35], an "evolutionary hotspot" for parallel flowering time adaptation
157 in *A. thaliana*, barley and rice[36] (fig. 2A;B; table S6). Candidate SNPs in *ELF3* are restricted to
158 high-latitude populations in both ranges, where they occur at moderate to high frequencies (fig.
159 2C). While the latitudes of these populations are greater in Europe than North America, the
160 climatic conditions are similar (fig. S3), indicative of local climate adaptation in parallel between
161 ranges. Additionally, a haplotype containing four nonsynonymous SNPs in an S-locus lectin
162 protein kinase gene was associated with several traits including flowering end date and
163 maximum height (fig. S2; table S6).
164

165 **Environmental-allele associations**

166 To identify genome-wide spatial signatures of local adaptation in North American and European
167 ranges, we performed genome scans for population allele frequencies among *A. artemisiifolia*
168 modern samples that were both highly divergent between populations (BayPass XtX)[37], and
169 correlated with 19 WorldClim temperature and precipitation variables (table S7)[38]. Statistics
170 were analyzed in 10kbp windows using the Weighted-Z Analysis (WZA)[39]. In North America
171 (143 samples; 43 populations), 2,167 (80.1%) of the 2,704 outlier windows for genomic
172 divergence (XtX) were also outlier windows for at least one environmental variable (XtX-EAA),
173 while in Europe (141 samples; 31 populations), only 1,357 (50.3%) of the 2,697 XtX outlier
174 windows overlapped environmental variable outlier windows. Signatures of local adaptation
175 were much stronger in North America than Europe, with the North American range showing
176 more extreme XtX values (fig. 2C), as well as more XtX-EAA windows (fig. 2C; table S7). This
177 suggests that North American *A. artemisiifolia* exhibits greater population differentiation, and a
178 stronger relationship between population differentiation and the environment than Europe, which
179 is consistent with the expectation that populations from the native range will be better-adapted
180 to their environment than those from the recently-invaded European range.
181

182 Previous studies in *A. artemisiifolia* have identified signatures of repeatability between native
183 and invasive ranges at phenotypic and genetic levels[10,14]. We observed congruent patterns in
184 our data: among North American and European XtX-EAA outlier windows, 291 showed parallel
185 associations with the same environmental variable between ranges (significantly more than
186 would be expected by chance; hypergeometric $p = 1.07\times10^{-126}$; fig. 2C), with 21.4% of climate
187 adaptation candidates in Europe also candidates in North America. To account for the possibility
188 that the number of parallel windows is inflated by extended linkage disequilibrium between
189 windows (and hence represents a smaller number of loci), we combined consecutive outlier
190 windows, and windows in haploblock regions, into single windows and repeated the analysis, in
191 which the parallelism remained highly significant (hypergeometric $p = 1.29\times10^{-91}$).
192 Consequently, many of the same regions of the genome are involved in climate adaptation in
193 both ranges.
194
195 North American, European and parallel XtX-EAA outlier windows included 28, 22, and three
196 flowering-time pathway genes, respectively, however this only represented a significant
197 enrichment (Fisher's exact test $p < 0.05$) in North America (table S8). GWAS flowering time
198 candidate *ELF3* was located in a parallel XtX-EAA window, while the flowering and height-
199 associated S-locus lectin protein kinase gene was in a North American XtX-EAA window only.
200 Gene ontology terms enriched in parallel XtX-EAA windows included "iron ion binding" and
201 "heme binding" (terms relating to cytochrome P450 genes), as well as "gibberellin biosynthetic
202 process" (table S9). Some cytochrome P450 genes are involved in detoxification of xenobiotic
203 compounds and the synthesis of defense compounds, while others play key developmental
204 roles[41], including contributing to the biosynthesis of gibberellin, a hormone that regulates a
205 range of developmental events including flowering[42].

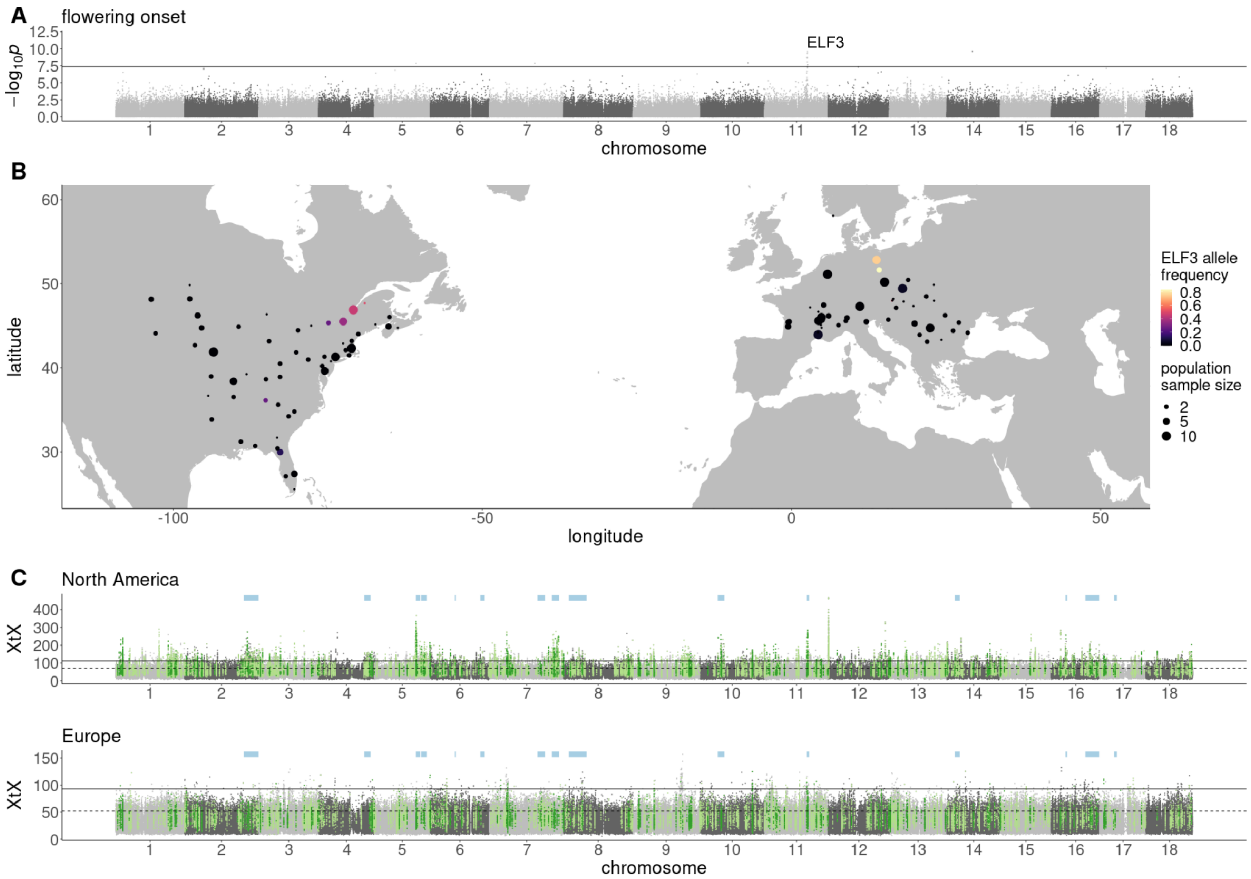

Figure 2. Signatures of climate adaptation in *Ambrosia artemisiifolia.* A. GWAS results (-$\log_{10}p$ against genomic location) for flowering onset (solid line indicates a Bonferroni-corrected p-value of 0.05). **B.** Distribution of a strongly-associated nonsynonymous SNP in *ELF3* among modern *A. artemisiifolia* populations used in this study. **C.** Genome-wide XtX scans between sampling locations within each range separately. Solid lines indicate Bonferroni-corrected significance derived from XtX *p*-values; dashed lines indicate the top 1% of genome-wide XtX values. Green highlights represent the top 5% of 10kbp WZA windows for each scan that are also among the top 5% of EAA WZA windows for at least one environmental variable, with dark green indicating outlier windows shared between North America and Europe. Pale blue bars indicate the location of 15 haploblocks (putative chromosomal inversions) that overlap shared outlier windows.

217 **Temporal phenotypic analysis**

218 To further identify the features of recent adaptation in *A. artemisiifolia*, we leveraged herbarium
219 samples, collected from as early as 1830, for phenotypic and genomic analyses. A trait-based
220 analysis of 985 digitized herbarium images (fig. S4) identified a significant shift in the probability
221 of flowering and fruiting over time in Europe, but this change depended on the latitude or the
222 day of the year the sample was collected (fig. S5; table S10). For the trait presence of a mature
223 male inflorescence, we identified a significant interaction between collection year and latitude
224 ($F_{1,886}$ = 7.89, p < 0.01) where in northern populations, more recently collected plants were more
225 likely to be flowering than older historic specimens. For this trait, collection day also significantly
226 interacted with collection year and more recently collected plants were more likely to be
227 flowering later in the year and less likely to be flowering earlier in the year. Similar patterns were
228 identified with the presence of fruit, as older samples were less likely to produce fruit later in the
229 season compared to recent samples (day-by-year interaction $F_{1,886}$ = 32.33, p < 0.001; fig. S5;
230 table S11). This substantial spatio-temporal change in phenology is consistent with
231 experimental common gardens that show that earlier flowering has evolved in northern
232 populations and later flowering in southern populations following the invasion of Europe[14].
233 Further, this shift in both flowering and fruit set over time supports the hypothesis that an initial
234 mismatch between the local environment and the genotypes present impacted the reproductive
235 output of *A. artemisiifolia* during the early stages of colonization, particularly in northern Europe.
236

237 **Genomic signatures of local selective sweeps**

238 Genome resequencing of *A. artemisiifolia* herbarium samples[11] allowed comparisons between
239 historic and modern populations. We grouped historic samples based on their age and proximity
240 to a modern population sample, resulting in five North American and seven European historic-
241 modern population pairs (table S12), which were scanned for signatures of local selective
242 sweeps by identifying windows with extreme shifts in allele frequency and extreme reductions in
243 diversity over time. We found far more evidence for recent sweeps in Europe (476 unique
244 windows) than in North America (129 unique windows; fig. S6 c.f. S7; table S12), consistent with
245 the expectation that a haphazardly-introduced invader will frequently be maladapted, initially,
246 and undergo rapid adaptation to local environmental conditions following its introduction. The
247 most dramatic selective sweep signature was observed in Berlin over a ~14Mbp region on
248 chromosome 2 (fig. 3A; fig. S7), which accounts for 274 (58%) of the European sweep windows.
249 In Berlin, sweep windows were also observed containing and surrounding the flowering onset
250 GWAS peak that includes *ELF3*. Scans of Fay and Wu's *H* in modern populations provide

251 further evidence for recent selection in these regions, and suggest more geographically
252 widespread selection in the region on chromosome 2 (fig. S8; S9). In comparisons of spatial and
253 temporal signatures of selection, three and five sweep windows were also XtX-EAA outliers in
254 North America and Europe respectively. All such windows in Europe were in the chromosome 2
255 or *ELF3* regions. To further investigate the temporal shift associated with *ELF3*, we focussed on
256 the nonsynonymous *ELF3* variant across all samples within a 200km radius of Berlin (15 historic
257 and eleven modern samples). The frequency of the variant increased from 2.6% to 73.9%
258 between historic and modern samples, an allele frequency shift greater than 10,000 putatively
259 neutral loci sampled from the same geographic region; similar shifts were not observed in North
260 American samples within a 200km radius of Quebec City (ten historic and eleven modern),
261 where the *ELF3* allele is at comparably high frequencies (fig. 3C).

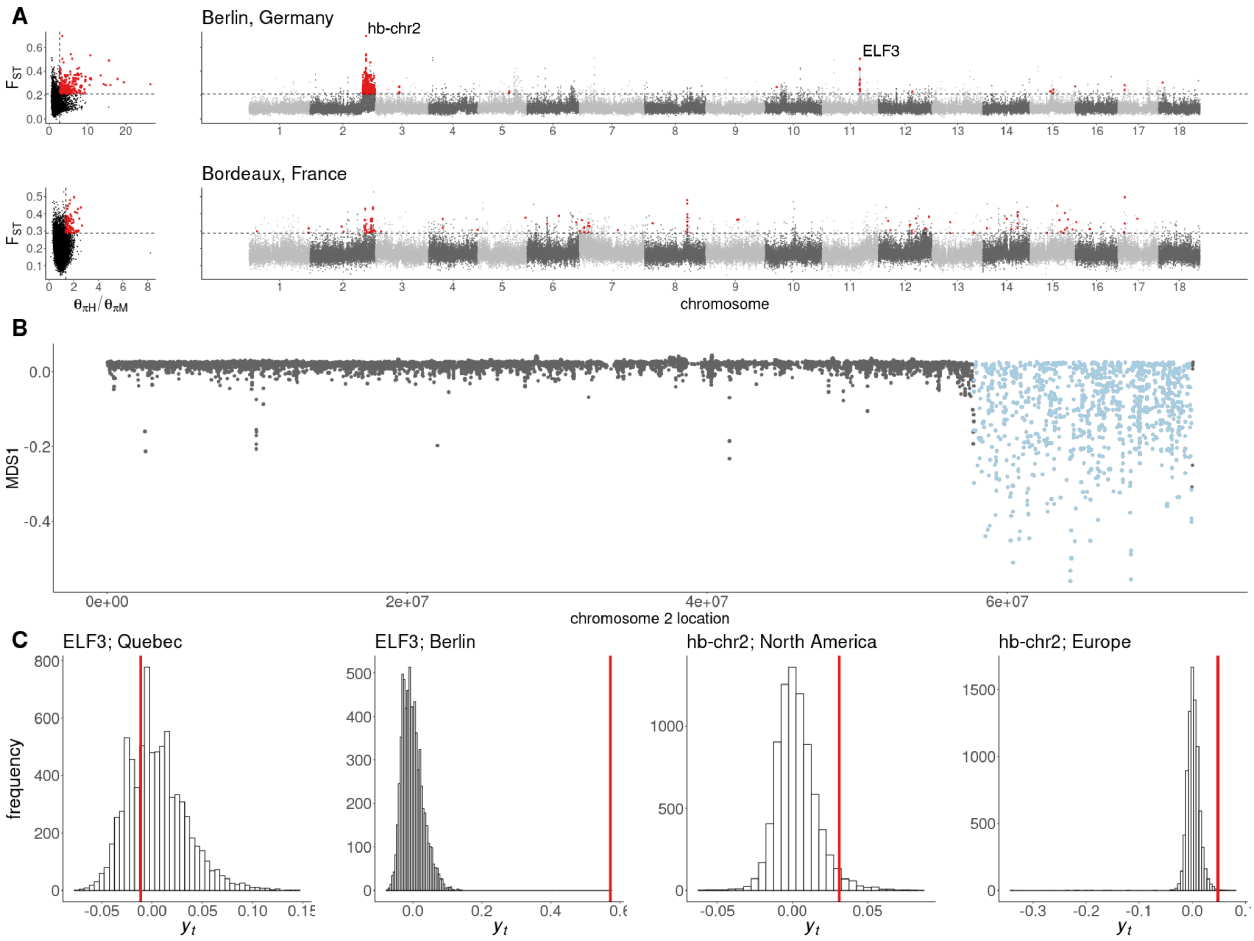

Figure 3. Temporal signatures of selective sweeps in Europe. A. Distributions of F_{ST} between historic and modern samples and the ratio of historic to modern nucleotide diversity ($\theta_{\pi H}/\theta_{\pi M}$) from Berlin and Bordeaux, and F_{ST} against genomic location. Red points indicate putative selective sweep windows, which are in the top one percent of per-window F_{ST} and $\theta_{\pi H}/\theta_{\pi M}$ (dashed lines). **B.** Strong evidence for a selective sweep on chromosome 2 in European populations corresponds with local divergent population structure (MDS1), indicating the presence of a haploblock (putative chromosomal inversion) in this region. **C.** A standardized measure of allele frequency change, y_t (calculated according to equation 1) for shifts between historic and modern populations across putatively neutral SNPs (histograms) and selective sweep candidates (red lines).

272 **Haploblock identification**

273 Chromosomal inversions have previously been identified as driving local adaptation of ecotypes
274 of *Helianthus* species[26]. We used a similar approach to identify genomic signatures of putative
275 inversions (haploblocks) contributing to local adaptation in *A. artemisiifolia*. Briefly, we identified
276 genomic regions in which population structure was divergent and fell into three clusters,
277 putatively representing the heterozygous and two homozygous genotypic classes of an
278 inversion. Further, we looked for pronounced shifts in population structure (indicating inversion
279 breakpoints), elevated local heterozygosity in the heterozygous cluster, and increased linkage
280 disequilibrium across the region (fig. S10). We examined mapping populations of *A.*
281 *artemisiifolia*[40] for evidence of map-specific reductions in recombination across haploblock
282 regions (i.e., suppressed recombination in haploblock regions in some maps but not others; fig.
283 S11). This would be the pattern expected when recombination is suppressed by inversions in
284 heterozygotes but not homozygotes, as opposed to the haploblocks being caused by global
285 reductions in recombination in those regions. Most haploblocks with sufficient markers in the
286 region showed evidence of suppressed recombination in some maps but not others, with the
287 exception of hb-chr6b, which showed suppressed recombination in all maps. To validate our
288 haploblock detection, we examined an alignment of our two haploid reference genomes and
289 identified four segregating inversion polymorphisms corresponding to haploblocks (fig 1B; fig.
290 S12).

291

292 Focussing our analysis on regions showing signatures of adaptation, we identified 15
293 haploblocks with the above genomic signatures of chromosomal inversions overlapping the 291
294 WZA windows that were parallel outliers for both XtX and at least one climate variable: hb-chr2
295 (14.5Mbp), hb-chr4 (6.2Mbp), hb-chr5a (4.1Mbp), hb-chr5b (5.4Mbp), hb-chr6a (1.1Mbp), hb-
296 chr6b (3.9Mbp), hb-chr7a (7.3Mbp), hb-chr7b (7.0Mbp), hb-chr8 (17.3Mbp), hb-chr10 (6.5Mbp),
297 hb-chr11 (2.2Mbp), hb-chr14 (4.9Mbp), hb-chr16a (1.7Mbp), hb-chr16b (13.7Mbp) and hb-chr17
298 (2.8Mbp). These haploblocks contained 77 of the 291 parallel XtX-EAA windows (26.5%; fig.
299 2C), although they only represent ~10% of the genome (a significant enrichment;
300 hypergeometric $p = 5.8\times10^{-17}$). One haploblock also corresponds to the European selective
301 sweep region on chromosome 2 (fig. 3A;B). This suggests that these haploblock regions have
302 played a pivotal role in generating parallel signatures of selection observed in *A. artemisiifolia*.

303

304 **Haploblock frequency changes through space and time**

305 To identify changes in haploblock frequency over time and space, which would be consistent
306 with selection on these putative inversions, we first estimated haploblock genotypes for all
307 historic and modern samples. Within haploblock boundaries identified using modern sample
308 SNP data in Lostruct[43], we performed local PCAs with both historic and modern samples (table
309 S4) and identified genotypes by kmeans clustering (fig. S9). For modern samples, we used
310 generalized linear models to estimate the slopes of the haploblock frequencies as a function of
311 latitude within each range. For those haploblocks that were significantly associated with latitude,
312 we compared these estimates with the genome-wide distribution of slopes for North America
313 and Europe, based on 10,000 unlinked SNPs that were randomly selected from outside
314 haploblocks and genes. The estimated slopes for eight haploblocks fell into the 5% tail of the
315 distribution for at least one of the ranges (fig. S13A). However, this approach did not examine
316 temporal changes nor the combined signatures of selection over space and time. To do so, we
317 ran generalized linear models comparing haplotype frequency with latitude, time (date of
318 specimen in years) and range (North America vs. Europe; fig. 4A; fig. S14; table S13-S18). All
319 but two (hb-chr6a and hb-chr7a) of the haploblocks showed significant changes over time,
320 space or both time and space. These patterns were robust to time being coded as discrete
321 (historic vs. modern) or as continuous (by year; table S13). Most showed temporal changes
322 either in their average frequency in one or both ranges, or in their relationship with latitude
323 within each range, a pattern that is consistent with recent local selection on these haploblocks.
324 Most of these haploblocks also showed significant associations with latitude in at least one
325 range or timepoint, indicative of climate adaptation. For instance, hb-chr10, hb-chr14, hb-chr16b
326 and hb-chr17 all showed significant parallel latitudinal associations in both ranges in historic and
327 modern samples. For hb-chr5b, haplotype frequency was negatively correlated with latitude in
328 modern and historic samples from North America, as well as in modern European samples,
329 consistent with climate-mediated selection. However, historic European populations did not
330 display an association with latitude, which may reflect maladaptation during the initial stages of
331 the European range expansion (fig. 4A; table S16, S18). In one case (hb-chr7b) the significant
332 latitudinal clines showed opposing yet significant slopes for each range in the modern samples,
333 perhaps indicating contrasting patterns of local selection between the ranges. For hb-chr2 the
334 latitudinal clines formed over time, with a substantial increase in frequency over time particularly
335 at higher latitudes.
336
337 To further investigate whether European populations showed evidence of recent local selection
338 on the haploblocks, we tested whether estimates of selection inferred from contemporary spatial

339 data were associated with temporal changes in haploblock frequencies between historical and
340 contemporary European populations. We used spatial variation in contemporary haploblock
341 frequencies to estimate the relative strength of local selection on these haploblocks (see
342 supplementary text S2). We specifically compared estimates of the maximum slope of latitudinal
343 clines for each putative inversion's frequency to simple population-genetic models for clines at
344 equilibrium between local selection and gene flow. In these models, cline slopes are
345 proportional to $\sqrt{s}/\sigma$, where s represents the strength of local selection for a given inversion and
346 σ is the average dispersal distance of individuals in the range[44] (supplementary text S2; table
347 S16). While our estimates of selection are, therefore, scaled by the dispersal rate, dispersal
348 should equally affect all inversions within a given range, allowing us to infer the relative strength
349 of spatially varying selection for each putative inversion. We found that estimates of the relative
350 strengths of local selection across the haploblocks in modern samples were correlated between
351 the ranges, indicating parallel patterns of local selection along the latitudinal gradient (r = 0.55, p
352 = 0.03). We also found that changes in the haploblock cline slopes between historic and modern
353 time points within Europe were significantly correlated with our estimates of the relative strength
354 of spatially varying selection of the haploblocks across the European range (r = 0.86, p < 0.001
355 fig. S13B). Such a pattern is consistent with a scenario in which historical European populations
356 were not initially locally adapted (haploblock frequencies were initially far from local optima) and
357 where the haploblocks subject to relatively strong local selection exhibited the greatest temporal
358 changes in local frequency over the ensuing century. The same pattern was not observed in the
359 North American native range, whose historic populations are likely to have been consistently
360 closer to the local optima across the timescale of our analysis (r = 0.25, p = 0.36). Cline slopes
361 for latitude were also shallower in historic relative to modern European populations ($t_{10.38}$ = -
362 3.09, p = 0.01; mean absolute slope: historic EU = 0.05; modern EU = 0.14), but not so in North
363 America ($t_{17.81}$ = -0.37, p = 0.71), consistent with initial maladaptation in Europe, followed by
364 adaptation to local climates.
365
366 The hb-chr2 haplotype frequency dramatically increased in many populations over time,
367 particularly at mid to high latitudes, which encompassed the European populations and northern
368 North American populations (fig 4; tables S13;S18). Signatures of selective sweeps were
369 observed in the hb-chr2 region in European populations in historic to modern comparisons of
370 divergence and diversity (fig. 3A; fig. S7). In this same region, negative outlier values of Fay &
371 Wu's H relative to the genome-wide pattern were identified in three of the five North American
372 and six of the seven European locations, indicating an excess of high frequency derived SNPs

373 and implicating recent positive selection (fig. S8; S9). To further distinguish the effects of drift
374 from those of selection, we compared an empirical null distribution of allele frequency changes
375 over time in Europe using 8,303 SNPs matched for allele frequency (fig. 3C). Only 11 (0.13%) of
376 the 8,303 loci in this null distribution showed an allele frequency change greater than hb-chr2.
377 We then estimated strengths of selection for the putative inversion that are consistent with the
378 observed increase in frequency within the invasive range (see supplementary text S1). With
379 positive selection for the putative inversion, the estimated frequency shift at the center of the
380 European range is consistent with a 2.4% difference in fitness (95% CI = {1.5%, 3.3%}) between
381 individuals homozygous for the inversion relative to homozygotes for the alternative haplotype.
382 Scenarios of balancing selection require stronger selection to explain the inversion frequency
383 shift over time (see supplementary text S1). This estimate is smaller than many empirical
384 estimates of selection on individual loci in natural populations[45]. The greater timespan of our
385 samples facilitated detection of strong signals of selection for loci that would otherwise be
386 missed by the short time periods afforded by most temporal studies.
387
388 **Biological functions of haploblocks**
389 Several analyses provide evidence for the biological function of these putatively adaptive
390 haploblocks. From genome annotations, we found that haploblocks were collectively enriched
391 for flowering-time pathway genes (Fisher's exact test $p = 0.002$), although individually only hb-
392 chr5b was significantly enriched (Fisher's exact test $p = 0.001$;table S8), consistent with a large-
393 effect flowering time QTL identified within this haploblock[40]. hb-chr2 was enriched for the
394 "recognition of pollen" gene ontology term, with 36 (17%) of the genome's 210 genes annotated
395 with this term falling within this haploblock (table S9). hb-chr5a was enriched for genes with the
396 "pectate lyase activity" term, including the top BLAST hit for *Amba1* (99.7% identity, *E*-value =
397 0), which encodes the *A. artemisiifolia* protein responsible for the majority of allergic reactions[46].
398 A detailed analysis of the hb-chr5a region reveals a cluster of six closely-related pectate lyase
399 genes, which correspond with elevated XtX and XtX-EAA outlier windows in both ranges (fig.
400 S15). hb-chr11 also overlaps the flowering time GWAS candidate *ELF3* (fig. 2A;B), and the
401 nonsynonymous variant which displays strong patterns in GWAS is only observed on one of the
402 haploblock genotype backgrounds. We also identified phenotypic associations with haploblocks
403 by encoding haploblock genotypes into our GWAS pipeline. Significant associations ($p < 0.05$
404 Bonferroni-corrected for multiple testing across 15 haploblocks) were observed for four
405 haploblocks, including for traits related to flowering time (fig. 4B; table S19).

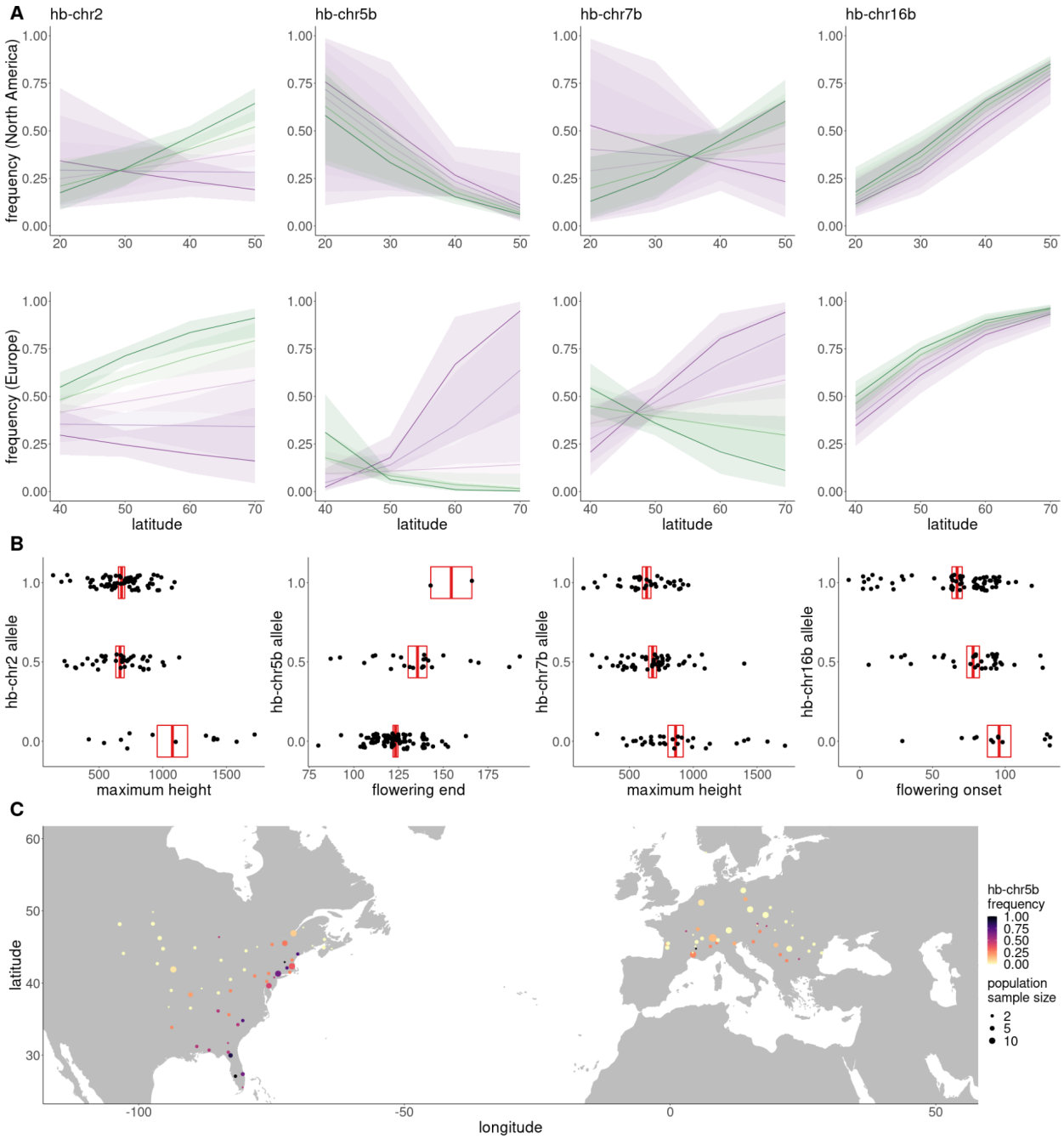

Figure 4. Haploblock distributions and trait associations. A. Logistic regression models with 95% CI ribbons (see table S13-18 for model details) of haploblock frequency (allele 1) against latitude for four haploblocks across five time bins ranging from most historic (purple) to most modern (green). **B.** Examples of significant associations between haploblock alleles and phenotypes (boxes denote mean and SEM). **C.** hb-chr5b allele frequency in modern *A. artemisiifolia* populations.

412 **DISCUSSION**

413 We have described, at unprecedented temporal and spatial resolution, the evolutionary-genetic
414 changes accompanying a recent and rapid invasion by a noxious pest. Our study system, while
415 unique in many ways, yields results with important general implications for our understanding of
416 the genetic basis of rapid adaptation to environmental change and the pervasiveness of parallel
417 evolution in geographically widespread species.
418
419 While invasive species are often envisaged to encounter novel selection pressures as they
420 spread across alien landscapes, they must also readapt to similar environmental variation
421 encountered in their native range, as haphazardly-introduced invaders are unlikely to be well-
422 adapted to local conditions when the invasive populations initially expand across climatic
423 gradients. Much of *Ambrosia artemisiifolia*'s European invasion lies within climatic extremes
424 encountered across its native range (fig. S3). Despite this similarity in climatic variation, the
425 patterns of parallel climate adaptation between native and invasive ranges are striking given the
426 evolutionarily recent introduction of the species into Europe. As *A. artemisiifolia*'s invasion of
427 Europe consisted of multiple introductions over a brief evolutionary time scale, these patterns
428 are likely examples of 'collateral evolution'[47], in which standing genetic variation in *A.*
429 *artemisiifolia*'s native range has been co-opted for adaptation in and across the European
430 invasive range. Parallel evolution is a hallmark of natural selection and parallel changes at the
431 genetic level point to constraints and biases in the genetic pathways to adaptation that are
432 evolutionarily achievable; when certain paths to adaptation are favored, such as when beneficial
433 variants are already present in the population as standing variants, evolution will repeatedly
434 draw on the same subset of genes to reach the same adaptive endpoints.
435
436 From herbarium specimens that were sampled throughout the course of *A. artemisiifolia*'s
437 invasion of Europe, we observed an abrupt change in flowering and fruiting over time.
438 Leveraging whole-genome sequences of herbarium samples across North America and Europe,
439 we were also able to scan populations for temporal genomic signatures of selective sweeps.
440 Although some populations have experienced shifts in ancestry over time in Europe[11], peaks
441 against the genome-wide background provide compelling evidence for rapid local adaptation in
442 European populations, with the strongest genetic signals of rapid change over time
443 corresponding to some of the strongest signatures of local adaptation in our spatial analyses,
444 particularly windows in the region of the *ELF3* gene and hb-chr2. Further, these regions show
445 parallel signals of climate adaptation in North America and are associated with adapting traits

446 such as flowering onset. These multiple lines of evidence provide strong support that climate-
447 mediated selection on phenology was pivotal in shaping the adaptive genetic landscape of *A.*
448 *artemisiifolia* in Europe.
449
450 Large haploblocks (putative inversions) contribute substantially to these genetic signals of
451 parallel adaptation. 27% of these haploblocks correspond to inversions segregating in our
452 diploid assembly. We propose that these haploblocks maintain cassettes of co-selected genes
453 that effectively segregate as single alleles of large effect[22,27], providing a genetic architecture
454 suited to local adaptation in the face of high gene flow[11,19]. Consistent with this hypothesis,
455 haploblocks are enriched for genes with particular biological functions, display associations with
456 locally-adaptive traits, and carry signals of strong selection in both the native and invasive
457 ranges. The evolution of inversions along environmental gradients has been reported in a range
458 of species[23]. However, by investigating haploblocks in an invasive plant with extensive
459 timestamped collections, we have demonstrated dramatic and adaptive evolutionary change of
460 inversions under natural conditions, providing compelling evidence of strong and recent natural
461 selection. These data have also allowed us to estimate selection for these variants, and we
462 have shown that haploblocks with the strongest estimates of clinal selection are driven more
463 rapidly towards their putative equilibria within the invasive range.
464
465 An important question during this era of environmental upheaval is the role of adaptation during
466 range expansion and its necessity during colonization. Through our analysis of historic samples,
467 we have shown that *A. artemisiifolia* was present in regions throughout Europe well before
468 many of these adaptive variants became locally common, suggesting the species' extensive
469 phenotypic plasticity may have facilitated its initial expansion. Strong local selection further
470 improved the match between genotypes and local environments, even appearing to affect
471 reproductive output in herbarium specimens. Many of the selected variants we identified are
472 linked to traits that are key factors in the timing, length and severity of the local pollen season
473 (e.g. days to flowering onset, days to the end of pollen production, and biomass). Consequently,
474 local adaptation has played a central role in shaping the allergy season in Europe and will likely
475 continue to be critical as climate change and continued range expansion further amplify the
476 damaging effects of this hazardous weed[48].

METHODS

Genome assembly

Seeds collected from a wild *Ambrosia artemisiifolia* population in Novi Sad, Serbia (lat. 45.25472, lon. 19.91231) were sown in potting soil at a greenhouse facility at the Ringve Botanical Garden, NTNU University Museum (Trondheim. Norway). After 160 days of growth under stable light and watering conditions, young leaf tissue from mature individual plant "NSS02/B" was sampled and flash-frozen in liquid nitrogen. These tissues were then shipped to Dovetail Genomics for high molecular weight DNA extraction and library building.

DNA samples were quantified using Qubit 2.0 Fluorometer (Life Technologies, Carlsbad, CA, USA). The PacBio SMRTbell library (~20kbp mean insert length) for PacBio Sequel was constructed using SMRTbell Express Template Prep Kit 2.0 (PacBio, Menlo Park, CA, USA) using the manufacturer recommended protocol. The library was bound to polymerase using the Sequel II Binding Kit 2.0 (PacBio) and loaded onto PacBio Sequel II). Sequencing was performed on PacBio Sequel II 8M SMRT cells generating 65.9Gbp of data. These PacBio CCS reads were used as an input to Hifiasm[49].

For each Dovetail Omni-C library, chromatin was fixed in place with formaldehyde in the nucleus and then extracted. Fixed chromatin was digested with DNAse I, chromatin ends were repaired and ligated to a biotinylated bridge adapter followed by proximity ligation of adapter containing ends. After proximity ligation, crosslinks were reversed and the DNA purified. Purified DNA was treated to remove biotin that was not internal to ligated fragments. Sequencing libraries were generated using NEBNext Ultra enzymes and Illumina-compatible adapters. Biotin-containing fragments were isolated using streptavidin beads before PCR enrichment of each library. The library was sequenced on an Illumina HiSeqX platform to produce ~30x sequence coverage. The PacBio CCS reads and Omni-C reads were then used as input for Hifiasm to produce two haplotype-resolved assemblies (hap1 and hap2) using default parameters.

HiRise was used (see read-pair above) to scaffold each haplotype-resolved assembly. Each *de novo* assembly and Dovetail OmniC library reads were used as input data for HiRise, a software pipeline designed specifically for using proximity ligation data to scaffold genome assemblies[28]. Dovetail OmniC library sequences were aligned to the draft input assembly using bwa[50]. The separations of Dovetail OmniC read pairs mapped within draft scaffolds were analyzed by HiRise to produce a likelihood model for genomic distance between read pairs, and the model

511 was used to identify and break putative misjoins, to score prospective joins, and make joins
512 above a default threshold (fig. S1C). The NCBI[51] genome submission portal identified 30
513 (7.4Mbp total) and 26 (6.4Mbp total) scaffolds in haplotypes 1 and 2 respectively containing
514 bacterial contamination which were subsequently removed from the final assembly.
515
516 We used GenomeScope 2.0 to estimate the genome size and ploidy using 21mers identified in
517 the reads with Jellyfish 2.3.0[52]. Genomescope estimated the haploid genome size to be
518 1.04Gbp using a diploid model (fig. S1A), a better model fit (95%) than the tetraploid model
519 (91%), which also vastly underestimated the haploid genome size (497 Mbp). This finding was
520 consistent with the smudgeplot produced by Genomescope, which also indicated diploidy (fig.
521 S1B). The final assembly sizes for each haplotype were 1.11 and 1.07Gbp, which were similar
522 to the GenomeScope estimates. BUSCO (Benchmarking Universal Single-Copy Orthologs)
523 version 5.1.3[31] analysis of each assembly using the eukaryota odb10 dataset (table S1)
524 demonstrated that both assemblies were complete with relatively low levels of duplication given
525 the history of whole genome duplication in the tribe.
526
527 To assess the presence of remnant haplotigs and other assembly artifacts, we mapped Illumina
528 reads used in the reference genome assembly to haplotype 1 of the reference genome using
529 AdapterRemoval[53], BWA-MEM[50] and Picard MarkDuplicates
530 (https://broadinstitute.github.io/picard/), and measured average sequencing depth and
531 heterozygosity of the alignment in non-overlapping 1Mbp windows across the genome. Window
532 depth was never greater than two times higher or 0.5 times lower than the mean, and
533 furthermore regions of both low depth and low heterozygosity were distributed throughout the
534 genome. The fact that there were no large regions with both low read-depth and low
535 heterozygosity points to the success of the haplotype-resolved assembly (fig. S1D). Minimap2
536 was used to align each haplotype against itself and against one another, after filtering for
537 alignments shorter than 10kbp and with fewer than 5000 matches, to identify homologous
538 blocks that may represent haplotigs. This analysis revealed the presence of a misassembly
539 where each assembly contained a region of scaffold 18 duplicated on scaffold 19, while the
540 orthologous region was missing in the alternative assembly. This suggested that a section of
541 scaffold 18 in each haplotype-resolved assembly had been incorrectly placed in the wrong
542 haplotype (corresponding to chromosome 18 in haplotype 1 and chromosome 9 in haplotype 2).
543 After making these manual corrections, the genetic map confirmed the continuity of these
544 chromosomes in each haplotype (fig. S16). The alignments of the final corrected assemblies

545 within and between the assemblies further confirmed the continuity of the assemblies and the
546 absence of haplotigs (fig. 1B).
547
548 **Whole-genome resequencing samples**
549 Whole-genome resequencing data used in this study have previously been described in Bieker
550 *et al.*[11]. Modern samples were field-collected between 2007 and 2019, and historic samples
551 were sequenced from herbarium specimens collected between 1830 and 1973. 121 modern
552 samples with corresponding phenotype data collected by van Boheemen, Atwater and
553 Hodgins[14] were used for genome-wide association studies. 284 modern samples (from
554 populations with a sample size >= 2) were used for environmental-allele associations. 97
555 historic and 100 modern samples divided into twelve populations were used for historic-modern
556 population comparisons (table S12). For *ELF3* analysis, 26 samples from within 200km of Berlin
557 (15 historic and eleven modern) and 21 samples within 200km of Quebec City (ten historic and
558 eleven modern) were used. Genotyping and analysis of haploblocks was performed using 311
559 modern and 305 historic samples. For details of each sample see table S5.
560
561 **Sample alignment, variant calling and filtering**
562 FASTQ files from historic and modern *A. artemisiifolia* samples from North America and
563 Europe[11] were aligned to haplotype 1 of our new reference genome using the Paleomix
564 pipeline[54], which incorporates AdapterRemoval[53], BWA-MEM[50], Picard MarkDuplicates
565 (https://broadinstitute.github.io/picard/) and GATK IndelRealigner[55]. Mean depths of alignments
566 ranged from 0.37X to 19.95X with a mean of 4.05X for historic samples, and 1.75X to 44.03X
567 with a mean of 6.86X for modern samples (table S5). Variants were called in the higher-depth
568 modern samples using GATK UnifiedGenotyper[56] on all contigs greater than 100kbp in length.
569 GATK VariantFiltration[55] and VcfTools[57] were used to filter variant calls. SNP and indel calls
570 were separately filtered using GATK hard-filtering recommendations (SNPs: QD < 2.0, FS >
571 60.0, SOR > 3.0, MQ < 40.0, ReadPosRankSum < -8.0, MQRankSum < -12.5; indels: QD < 2.0,
572 FS > 200.0, SOR > 10.0, ReadPosRankSum < -20.0, InbreedingCoeff < -0.8). Additionally,
573 SNPs and indels were separately filtered for sites with depth (DP) less than one standard
574 deviation below the mean, and greater than 1.5 standard deviations above the mean. Individual
575 genotypes were set to missing if their depth was less than three, then variants with greater than
576 20% missing across all samples were removed. Samples with greater than 50% missing
577 variants were removed. For the remaining 311 modern samples, genotypes were phased and
578 imputed using Beagle 5.2[58].
579

580 **Genome annotation**

581 To obtain RNA transcript sequences for annotation of the genome, after 160 days of growth
582 additional samples of leaf, stem, flower, root, and branch were taken from individual "NSS02/B"
583 and flash-frozen in liquid nitrogen. From these we extracted RNA from seven tissues (young
584 leaf, old leaf, stem, branch, and three stages of development of the floral head) using a
585 Spectrum Plant Total RNA Kit (Sigma, USA) with on-column DNA digestion following the
586 manufacturer's protocol. RNA extracts from all five tissues were pooled into a single sample.
587 mRNA was enriched using oligo (dT) beads, and the first strand cDNA was synthesized using
588 the Clontech SMARTer PCR cDNA Synthesis Kit, followed by first-strand synthesis with
589 SMARTScribeTM Reverse Transcriptase. After cDNA amplification, a portion of the product was
590 used directly as a non-size selected SMRTbell library. In parallel, the rest of amplification was
591 first selected using either BluePippin or SageELF, and then used to construct a size-selected
592 SMRTbell library after size fractionation. DNA damage and ends were then repaired, followed
593 by hairpin adaptor ligation. Finally, sequencing primers and polymerase were annealed to
594 SMRTbell templates, and IsoSeq isoform sequencing was performed by Novogene Europe
595 (Cambridge, UK) using a PacBio Sequel II instrument, yielding 97,819,215 HiFi reads. To
596 prepare the raw IsoSeq RNA data for downstream use in the annotation of the genome, we first
597 identified the transcripts in the PacBio single-molecule sequencing data by following the IsoSeq
598 v3 pipeline provided by PacificBiosciences (https://github.com/PacificBiosciences/IsoSeq).
599 Briefly, the pipeline takes PacBio subread files as an input and undergoes steps of consensus
600 generation, demultiplexing of primers, IsoSeq3 refinement, followed by a final clustering of the
601 reads.
602
603 Prior to annotation of the genome, repetitive elements were identified using RepeatModeler2[59].
604 ProExcluder[60] was then run to remove any protein coding genes from the repeat library.
605 RepeatMasker[61] was used to mask the genome using the finalized repeat library (table S3). A
606 large fraction of the genome consisted of repetitive sequence (66.51%; fig. 1A). Retroelements
607 were the largest class (39.13%), with long terminal repeats, particularly Gypsy (7.73 %) and
608 Copia (18.82 %), the most prevalent retroelements.
609
610 Genome annotation was performed using the MAKER v.3.01.03 [62] pipeline. Genome assembly
611 fasta file, the custom repeat library, IsoSeq clustered reads merged with a previously described
612 transcriptome[11] (as expressed sequence tag [EST] evidence) and protein homology evidence
613 from a plant protein database which combines the Swissprot plant protein database and NCBI

614 Refseq for plants excluding transposable elements were used as the input files for the first run
615 of the annotation pipeline. The custom repeat library was used to mask the repetitive regions.
616 Additional regions with low complexity were soft masked using RepeatMasker v.4.1.1 [61]**.** Gene
617 predictors SNAP v.2013-11-29 [63] and AUGUSTUS v.3.3.3 [64] were trained by running iterative
618 runs of Maker as recommended by [62]**.** As the first round of annotation was based on the
619 alignment of the EST evidence to the genome, est2genome option in the Maker control file was
620 set to one to allow Maker to infer gene models directly from the EST evidence. After the
621 completion of the first round of annotations, gene models with an AED (Annotation Edit
622 Distance) score of 0.25 or greater and a length of 50 or more amino acids were retained and
623 used to train SNAP v.2013-11-29 [63] to obtain a SNAP hmm file. We then trained AUGUSTUS
624 v.3.3.3 [64] using BUSCO v.3.0.2 [65]. First, training sequences were identified using the gene
625 models predicted by Maker from the first run by excising regions with mRNA annotations and
626 1000 bp on either side. These were used to run BUSCO using the embryophyte set of
627 conserved genes. After training both SNAP and Augustus, Maker was run again, with SNAP
628 hmm and Augustus files. A total of three rounds of training for each gene predictor were run. We
629 used the script genestats [66] to calculate the numbers and lengths of genes, exons, introns and
630 UTR (untranslated region) sequences present in the predicted gene models by the final Maker
631 run. We ran BUSCO v.5.1.3 [31] with the eukaryota_odb10 lineage data set on the predicted
632 transcript fasta file by Maker to assess the quality and the completeness of the annotated
633 genome.
634
635 For haplotype 1, a high confidence gene set of 36,826 gene models with strong protein or
636 transcript support was identified (table S4). Gene models were compared with *Arabidopsis*
637 *thaliana* annotations (TAIR10 representative gene model proteins[67]) and the UniProtKB plants
638 database using the *blastp* command in BLAST+[68]. Using an *E*-value threshold of 1×10^{-6}, 32,370
639 (87.9%) genes matched TAIR10 annotations and 28,092 (76.3%) matched UniProtKB. We
640 identified 98.4% of the core eukaryotic genes amongst our annotated genes, 73.3% being single
641 copy, 20% being duplicated and 5.1% fragmented compared to BUSCO markers present in the
642 library *eukaryota_odb10.2020-09.10* (fig. 1C). Gene ontology (GO) enrichment was assessed
643 using GO terms from *A. thaliana* TAIR 10[67] BLAST results. To identify GO terms enriched
644 among candidate lists, the R/topGO package[69] was used with Fisher's exact test, the 'weight01'
645 algorithm, and a *p*-value < 0.05 to assess significance. Additionally, annotations were cross-
646 referenced with 306 *A. thaliana* FLOR-ID flowering time pathway genes[70]. 513 predicted *A.*
647 *artemisiifolia* genes were matched to this dataset, representing 218 unique FLOR-ID genes.

648 Enrichment of flowering time genes was also assessed in candidate gene lists using Fisher's
649 exact test and a $p < 0.05$ threshold. The effects of imputed variants on predicted genes were
650 estimated using SnpEff[71].
651
652 **Allele frequency outliers and environmental allele associations**
653 Imputed genotype data from modern samples were divided for between-range and within-range
654 analyses in PLINK 1.9[72], and a minor allele frequency threshold of 0.05 was applied within data
655 subsets. For within-range analyses, sampling locations with fewer than two samples were
656 excluded and allele frequencies were calculated for each sampling location, resulting in
657 1,150,328 SNPs across 143 samples and 43 populations in North America and 1,132,342 SNPs
658 across 141 samples and 31 populations for Europe. Allele frequency outliers were identified
659 within each range using the BayPass core model[37], with an Ω covariance matrix computed from
660 10,000 randomly-sampled SNPs that were located outside annotated genes and haploblocks,
661 and pruned for linkage disequilibrium using a window size of 50kb, a step size of 5bp and an r^2
662 of 0.5 in PLINK[72]. To identify allele frequency variation associated with environmental variables
663 within ranges, 19 bioclimatic variables were extracted for each sampling location from the
664 WorldClim database[38] using the R/raster package[73]. Population allele frequencies were
665 assessed for correlation with 19 bioclimatic variables using Kendall's τ statistic in R[74]. Genome-
666 wide XtX and τ results were analyzed in non-overlapping 10kbp windows using the weighted-Z
667 analysis (WZA)[39], with the top 5% of windows designated outliers.
668
669 **Genome-wide association studies**
670 Imputed genotypes from modern samples were filtered in PLINK 1.9[72]. Non-SNP sites and sites
671 with more than two alleles were removed. The 121 samples overlapping those phenotyped by
672 van Boheemen, Atwater and Hodgins[14] were retained (table S5), and sites with a minor allele
673 frequency below 0.05 were removed, resulting in 1,142,278 SNPs for analysis. Genome-wide
674 association studies (GWAS) were performed across 121 individuals from both North American
675 ($n = 43$) and European ($n = 78$) ranges using EMMAX[75], and incorporating an identity-by-state
676 kinship matrix (generated in PLINK 1.9)[72] to account for genetic structure among samples. The
677 kinship matrix was computed using 790,209 SNPs which remained after pruning for linkage
678 disequilibrium using a window size of 50kb, a step size of 5bp and an r^2 of 0.5. Candidate SNPs
679 were identified using a conservative threshold of Bonferroni-corrected p-values < 0.05.
680
681 **Phenotypic analysis of herbarium specimens**

682 We conducted a trait-based analysis of herbarium specimens found in the Global Biodiversity
683 Information Facility database (gbif.org 2021). We compiled information from all *A. artemisiifolia*
684 European herbarium specimens for which there was a digitized image of the individual in the
685 database alongside corresponding metadata (location and collection date). The collection date
686 spanned 1849 to 2020 (median 1975) and comprised 985 specimens. We determined the stage
687 of flowering (no male inflorescence present, only immature male inflorescence present, mature
688 male inflorescence present) for each image. The presence of fruit was also recorded. The male
689 inflorescence was used as an indicator of flowering as these structures are more visually
690 prominent than female flowers and the onset of male and female flowering is highly correlated[14].
691 Male florets consist of prominent spike-like racemes of male capitula, and are found at the
692 terminus of the stem, whereas female florets are observed to be in inconspicuous cyme-like
693 clusters and are arranged in groups at the axils of main and lateral stem leaves (fig. S4). The
694 dates when the specimens were collected were converted to Julian day of the year. We
695 conducted a generalized linear model with a binomial response and logit link (glm R). Both
696 binary traits (presence of a mature male inflorescence; the presence of fruit) were included as
697 response variables in two separate models. The significance of the effects were tested using the
698 *Anova* function (Car package R)[76] using type 3 tests. For both models, the predictors of latitude,
699 day of the year, and collection year as well as all interactions were included. Non-significant
700 interactions were removed in a stepwise fashion, starting with the highest order. Latitude of
701 origin strongly correlates with flowering time in common garden experiments[14] and we expected
702 northern populations to evolve early flowering relative to the start of the growing season to
703 match the shorter growing seasons in these areas. As a result, if local phenology has evolved to
704 better match the local growing season we predicted a collection year by latitude interaction, as
705 the relationship between latitude and the probability of flowering in wild collected accessions
706 should change over time when controlling for the day of collection.
707
708 **Historic-modern genomic comparisons**
709 To identify targets of recent selection, we compared historic and modern samples from twelve
710 locations (five locations from North America and seven from Europe; table S12). Historic
711 samples were grouped based on age of sample and proximity to a modern population. Analyses
712 were performed in ANGSD[77] using genotype likelihoods. For each population location we
713 calculated pairwise nucleotide diversity (θ_π) for historic and modern populations separately, and
714 F_{ST} between historic and modern populations at each location. Statistics were calculated in non-
715 overlapping 10kbp windows, and windowed θ_π values were normalized by dividing by the

716 number of sites in each window. At each location, windows with θ_π more than two standard
717 deviations below the mean in both historic and modern populations were excluded from the
718 analysis. We identified putative selective sweeps in each population as windows with extreme
719 shifts over time in allele frequency as well as extreme reductions in diversity (i.e. windows in the
720 top one percent of both F_{ST} and $\theta_{\pi H}/\theta_{\pi M}$ distributions). To obtain further evidence for selective
721 sweeps in these populations, we also performed genome scans of Fay and Wu's H in each
722 modern population. We first generated an ancestral consensus sequence in ANGSD (*-doFasta*
723 *2 -minMapQ 25 -minQ 20 -remove_bads 1 -uniqueOnly 1 -doCounts 1*) from alignments of
724 *Ambrosia carduacea* and *Ambrosia chamissonis* to our *A. artemisiifolia* reference genome. We
725 then used this ancestral sequence in calculating Fay and Wu's *H* in 10kbp windows in ANGSD.
726
727 **Temporal allele frequency shifts in candidate loci**
728 In order to track allele frequency shifts over time, we estimated contemporary and historical
729 allele frequencies of the *ELF3* non-synonymous SNP and the haploblock hb-chr2, which are two
730 candidate loci for recent selection in Europe. Both candidates showed evidence of local
731 selection using spatial analysis of modern populations, as well as sweep signals in temporal
732 comparisons of individual populations. These calculations were performed in geographic
733 regions where this recent selection is believed to have occurred at both historic and
734 contemporary timepoints. ANGSD[77] (*-minMapQ 10 -minQ 5 -GL 2 -doMajorMinor 1 -doMaf 2 -*
735 *doIBS 1 -doCounts 1 -doGlf 2*) was used to calculate the allele frequency of the early flowering
736 *ELF3* allele (11:41517231) in 15 historic and eleven modern samples from within 200km of
737 Berlin, whilst the frequency of hb-chr2 in Europe was ascertained using haploblock frequency
738 estimates from across the European range (see below). To understand the magnitude of these
739 allele frequency shifts relative to putatively neutral alleles elsewhere in the genome, we
740 calculated a standardized measure of frequency change, y_t, using estimates of historic, p_0, and
741 contemporary, p_t, allele frequencies according to the equation:
742
743
$$y_t = \frac{p_t - p_0}{\sqrt{tp_0(1 - p_0)}}$$
744
745 where *t* is the number of generations separating the frequency estimates (equivalent to the
746 number of years due to ragweed's annual lifecycle). As we show in supplementary text S3, the
747 distribution of y_t estimates under neutrality are predictable and roughly independent of the initial
748 frequency of each neutral variant once the loci with low-frequency initial minor allele frequencies

749 are filtered out. To further assess if selection was the likely cause of temporal changes of the
750 *ELF3* and hb-chr2 variants, we estimated the distribution of y_t estimates computed from 10,000
751 randomly-sampled SNPs that were located outside annotated genes and haploblocks and
752 pruned for linkage disequilibrium using a window size of 50kb, a step size of 5bp and an r^2 of
753 0.5 in PLINK 1.9[72]. Prior to calculation of y_t, sampled SNPs were then filtered for a minor allele
754 frequency > 0.2 for hb-chr2 comparisons and MAF > 0.05 for *ELF3* comparisons (due to the low
755 historic frequency of *ELF3* in historic Berlin populations), resulting in null distributions of
756 between 6,913 and 8,303 SNPs. We then compared the distributions to the y_t values of
757 candidate adaptation loci to test whether candidate regions were more divergent than the
758 putatively neutral distribution. As a point of comparison we repeated this analysis for hb-chr2 in
759 North America and the *ELF3* allele in Quebec. As in Berlin, the *ELF3* allele is at high
760 frequencies, but substantial temporal change was not expected as the populations were
761 predicted to be closer to the equilibrium over the temporal sampling period in the native range.
762 Samples within 200km of Quebec City (ten historic and eleven modern) were pooled at both
763 timepoints. Allele frequency changes of the 10,000 randomly-sampled SNPs and the non-
764 synonymous *ELF3* allele were assessed as above.
765
766 **Haploblock identification**
767 To identify signatures of large, segregating haploblocks across the genome, we performed local
768 windowed principal component analysis with Lostruct[43]. Using SNP data from 311 modern
769 samples, we extracted the first ten multidimensional scaling (MDS) coordinates across each
770 chromosome in windows of 100 SNPs. These MDS coordinates were then plotted along each
771 scaffold to observe regions of local structure, indicative of segregating haploblocks. We focused
772 on outlier MDS signals that overlapped parallel outlier windows for both XtX and at least one
773 environmental variable, and also showed well-defined boundaries indicative of chromosomal
774 inversions. We tested for additional evidence of inversions using PCA of MDS outlier regions
775 and kmeans clustering in R[74] to identify regions containing three distinct clusters representing
776 heterozygotes and two homozygotes. Additionally, we assessed heterozygosity from genotype
777 data in each haploblock region and in each modern sample, and measured linkage
778 disequilibrium (the second highest r^2 value in 0.5Mbp windows) across each scaffold bearing a
779 haploblock for all modern samples and for modern samples homozygous for the more common
780 haploblock genotype using scripts from Todesco *et al.*[26].
781
782 **Haploblock frequency changes over time and space**

783 For fifteen candidate inversions, a local PCA of each region and kmeans clustering was then
784 repeated in PCAngsd[78], so as to allow genotype estimation of these haploblocks in 305 historic
785 samples alongside the 311 modern samples. For this local PCA we used only the chromosomal
786 regions already defined as haploblocks in order to obtain population wide clustering for both
787 historic and modern datasets, which we then used to infer haploblock genotypes. We also
788 conducted a PCA on 10,000 SNPs randomly-sampled from the 311 modern genomes that were
789 located outside annotated genes and haploblocks, and pruned for linkage disequilibrium using a
790 window size of 50 kb, a step size of 5 bp and an r^2 of 0.5 in PLINK[72]. Following this, we used
791 generalized linear models (glm R) to assess how haplotype frequency (binomial response)
792 changed over time and space. A count of each haplotype at a geographic location and year was
793 the binomial response variable and time period (historic or modern), range (North America or
794 Europe), latitude, and all interactions between these three main effects were used as predictors.
795 Non-significant interactions were removed in a stepwise fashion, starting with the highest order.
796 PC1 from the PCA of 10,000 randomly-sampled SNPs was included as a covariate to control for
797 the effects of population structure on haplotype frequency. We tested the significance of the
798 effects in our model using the Anova function (Car package R)[76] with type 3 tests. Significant
799 differences among groups for means or slopes were tested with the emmeans package using
800 an FDR correction[79]. To determine if the classification of samples into modern or historic
801 timepoints influenced our results we ran a second set of generalized linear models examining
802 haplotype frequency as a function of collection year, range (North America or Europe), latitude,
803 and all interactions between these three main effects as well as PC1, using the same approach
804 as above. For interactions involving two continuous variables (i.e., latitude and year) we tested if
805 the slope estimates of one variable were significant at specific values of the other using the
806 package emmeans. This allowed us to estimate when and where the haplotype frequencies
807 were changing. The results from both approaches (time as two categories or time as
808 continuous) provided qualitatively similar patterns.
809
810 We estimated the relative strength of selection on haploblocks along the latitudinal clines in
811 modern North American and European populations using slopes from logistic regressions (see
812 supplementary text S2). Specifically, we used generalized linear models to estimate the slopes
813 of the regression for each range and time point (modern or historic) combination (group). A
814 count of each haplotype at a geographic location and collection year was the binomial response
815 variable and time period (historic or modern), range (North America or Europe), latitude, and all
816 interactions between these three main effects were used as predictors. All interactions were

817 retained in the model and slopes and their confidence intervals estimated for each group using
818 the function emtrends (emmeans package R[79]; table S14). PC1 was included as a covariate to
819 control for the effects of population structure on haplotype frequency. We expected the slopes to
820 be shallower in the historic versus the modern European group, but similar across timepoints in
821 North America. To test this, we used a t-test and compared slopes for modern and historic
822 timepoints in each range. We also expected that the magnitude of change in the slope over time
823 would be the greatest in haploblocks showing the largest estimates of selection in Europe (table
824 S16). We estimated the relative strength of selection for the modern European range for each
825 haploblock and tested if the absolute change in slope for each haploblock was correlated with
826 this estimate. We also examined if there was a correlation in the relative strength of selection for
827 modern North American and European haploblocks, which would indicate parallel selection
828 along the cline in each range.
829
830 We compared our slope estimates of the haploblocks to the genome wide distribution in each
831 range using 10,000 randomly selected SNPs outside of genes and haploblocks. We did this to
832 determine if our haploblocks showed stronger latitudinal patterns than the majority of SNPs, in
833 one or both ranges, which may be indicative of spatially varying selection. For the modern
834 samples in each range (North America or Europe), we fit a generalized linear model with latitude
835 as the only predictor. We did this for each null SNP and each haploblock that was statistically
836 associated with latitude.
837
838 **Recombination rates in haploblocks**
839 The haploblocks show multiple genomic signatures of reduced recombination. To confirm this
840 we analyzed recombination rates in genetic maps. Further if the haploblocks were caused by
841 global reductions in recombination rate (e.g., the region was found in an area with generally low
842 recombination such as a centromere), all maps should show reduced recombination rates.
843 However, if inversions were the cause, recombination would only be suppressed in genotypes
844 heterozygous for the inversion, while homozygous individuals would not show suppressed
845 recombination. To determine if there were genotype-specific reductions in recombination rate in
846 the haploblocks, which would be consistent with inversions, we made use of three previously
847 generated genetic maps[40]. Markers were generated using genotype by sequencing and
848 alignments to the haplotype 1 of our diploid reference genome. Details of the sequencing,
849 alignments and variant calling can be found in Prapas *et al.*[40]. We developed sex-specific
850 genetic maps (i.e., maps for the maternal and paternal parent) using Lep-MAP3[80] for each

851 chromosome of interest and in each mapping population (an F1 mapping population and two F2
852 mapping populations). Multiple maps were constructed since the haploblocks may have been
853 segregating in different frequencies in the parents of the mapping populations derived from
854 outcrossing. For the recombination rates, linkage map construction was constrained by the
855 physical order of the markers along each scaffold of interest. Genetic distance (cM) was plotted
856 against physical position along the chromosome for each map and the intervals of the QTL and
857 the boundaries of the haploblocks were visualized and inspected for reduced recombination
858 compared to the rest of the scaffold. We also used the genetic map (pink family) to confirm the
859 OmniC scaffolding, and assess the accuracy of the manual correction of chromosome 18 in
860 both assemblies (fig. S16).

ACKNOWLEDGEMENTS

We thank Greg Owens & Michael Whitlock for discussions, and Samuel Yeaman and Sarah Otto for feedback on the manuscript. We are grateful to François Bretagnolle, Myriam Gaudeul, Heinz Mueller-Schaerer, Gerhard Karrer, and Bruno Chauvel for their assistance in obtaining many of the samples upon which this study is based, and Marie Brunier, Fátima Sánchez Barreiro, Yohann Roy, Luna Forcioli, Jacqueline Y. Lee for assistance during lab work. Some sequencing services were provided by the Norwegian Sequencing Centre, a national technology platform hosted by the University of Oslo. Some sequencing was performed by the NTNU Genomics Core Facility. Genome scaffolding was performed by Dovetail Genomics. Some analyses were performed on resources provided by Sigma2, MASSIVE M3 and ComputeCanada high performance computing platforms. We kindly thank the curators from the following herbaria for allowing us to destructively sample their precious collections: B, BR, BRNU, C, FI, G, GH, GOET, GZU, HBG, I, IASI, JE, L, LD, LY, MARS, MASS, MO, MPU, NEBC, NEU, NY, P, PH, PR, PRA, PRC, QFA, S, STU, TRH, UPS, US, W, WU.

FUNDING

This research received support from an NTNU Onsager Fellowship award, Norwegian Research Council Young Research Talents award 287327, and a SYNTHESYS Project award (www.synthesys.info, financed by European Community Research Infrastructure Action under the FP7 "Capacities" Program) to M. D. M., a FORMAS (2016-00453) & Carl Trygger Foundation for Scientific Research (grant CTS 14.425) to R. S., and an ARC DP220102362 and DP180102531 and HFSP RGP0001/2019 to K. A. H .

AUTHOR CONTRIBUTIONS

Paul Battlay: Software, Formal analysis, Investigation, Data curation, Writing - Original draft, Writing - Review and editing, Visualization **Jonathan Wilson:** Software, Formal analysis, Investigation, Writing - Review and editing, Visualization **Vanessa C. Bieker:** Software, Investigation, Data curation **Chris Lee:** Investigation, Resources **Diana Prapas:** Software, Formal analysis **Bent Petersen:** Software **Sam Craig:** Investigation **Lotte van Boheemen:** Investigation, Resources **Romain Scalone:** Resources **Nissanka P. de Silva:** Software, Visualization **Amit Sharma:** Investigation, Resources **Bojan Konstantinović:** Investigation, Resources **Kristin A. Nurkowski:** Investigation, Resources **Loren Rieseberg:** Writing - Review and editing **Tim Connallon:** Methodology, Formal analysis, Investigation, Writing - Original

draft, Writing - Review and editing **Michael D. Martin:** Conceptualization, Methodology, Resources, Writing - Review and editing, Supervision, Project administration, Funding acquisition **Kathryn A. Hodgins:** Conceptualization, Methodology, Software, Formal analysis, Investigation, Resources, Writing - Original draft, Writing - Review and editing, Supervision, Project administration, Funding acquisition, Visualization

COMPETING INTERESTS

The authors declare no competing interests

DATA AND CODE AVAILABILITY

Sequences used in reference genome assembly and annotation are available from NCBI under BioProject ID PRJNA819156. Reference genome FASTA and annotation GFF files are available from FigShare (DOI TBA). Individual sample resequencing data are available from ENA under BioProject IDs PRJEB48563, PRJNA339123 and PRJEB34825.

SUPPLEMENTARY FIGURES

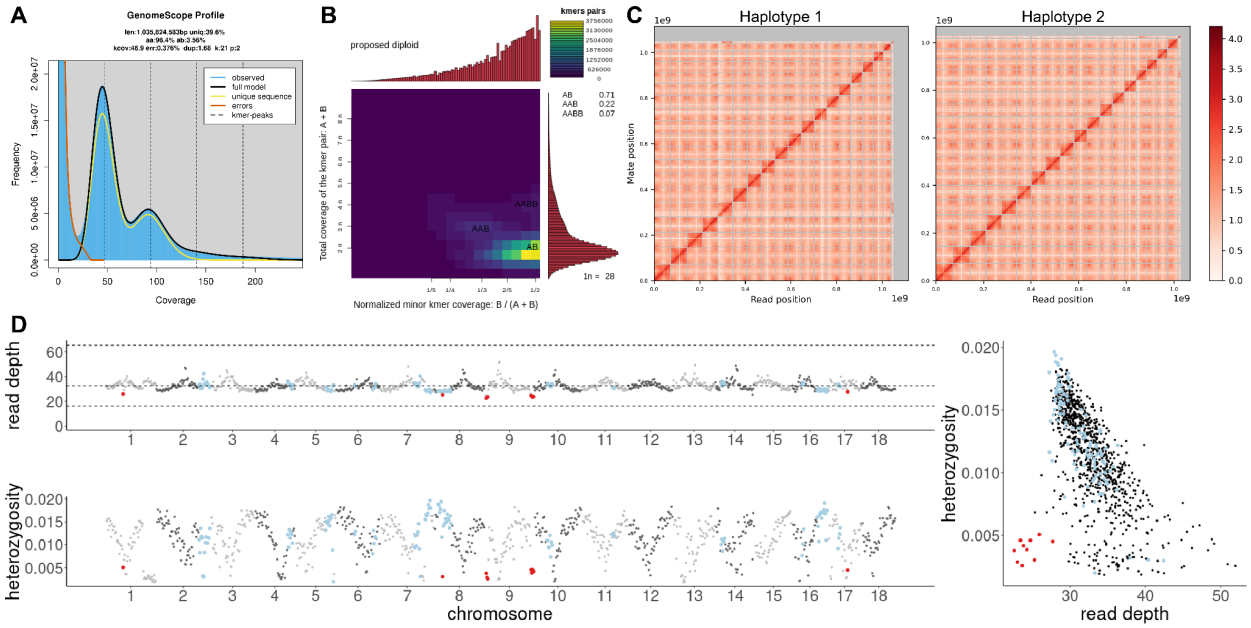

Figure S1. *Ambrosia artemisiifolia* genome assembly quality. A. The kmer coverage and model fit from GenomeScope 2.0 for 21mers from the PacBio HiFi and OmniC Illumina reads. **B.** A smudgeplot used to estimate ploidy from heterozygous kmer pairs using 21mers from the HiFi reads. **C.** Link density histograms, identified by proximity ligation sequencing for haplotype 1 and haplotype 2. The *x* and *y* axes show mapping positions of the first and second read in read pairs. **D.** Read depth and heterozygosity in 1Mbp windows for Illumina reads used in the reference genome assembly mapped to the final version of the reference genome. Windows in the bottom 10% of read depth and heterozygosity values are indicated in red; windows overlapping haploblocks are indicated in pale blue.

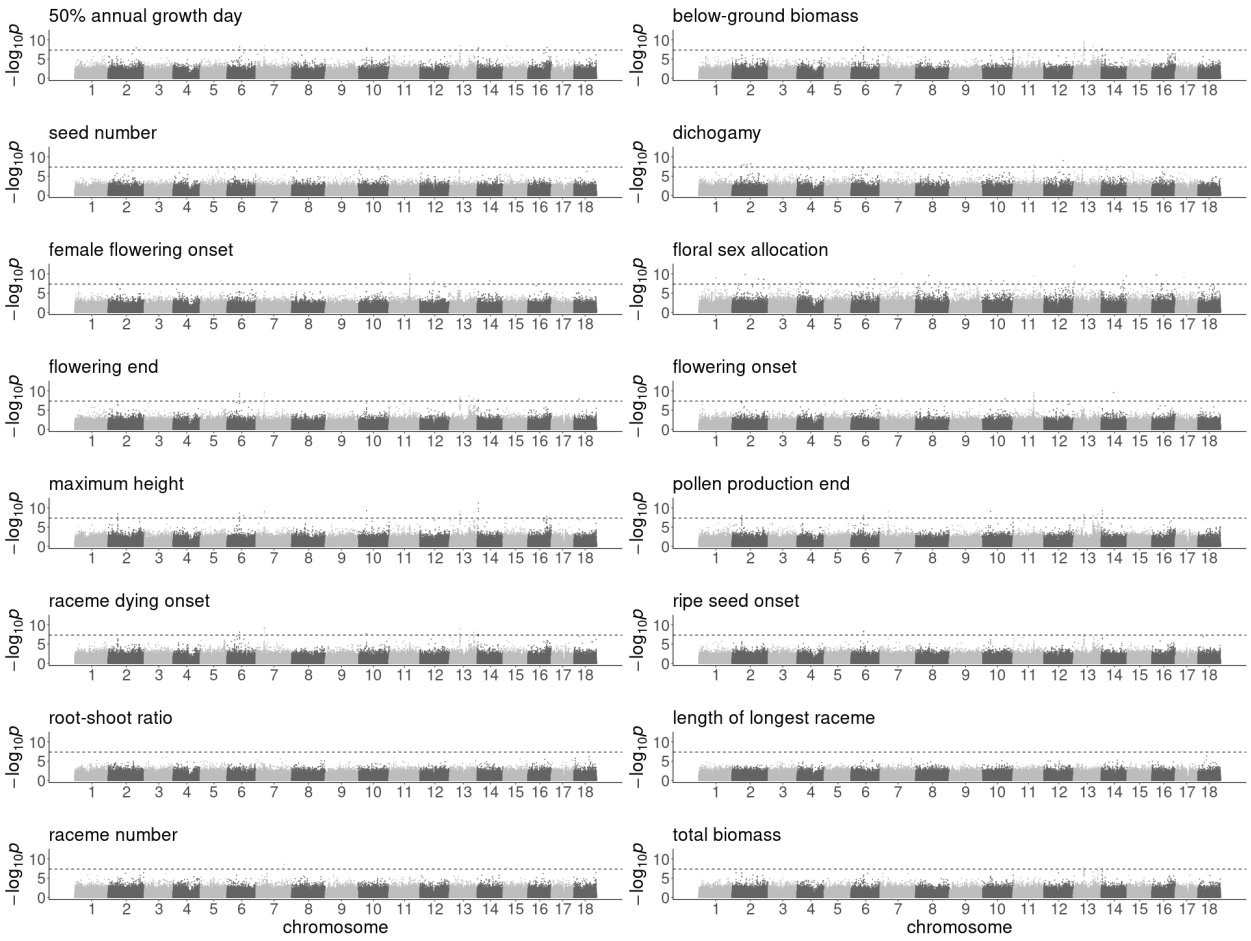

Figure S2. Genome-wide association study results for phenotypes with significant SNPs. Solid lines indicate a bonferroni-corrected significance threshold of 0.05.

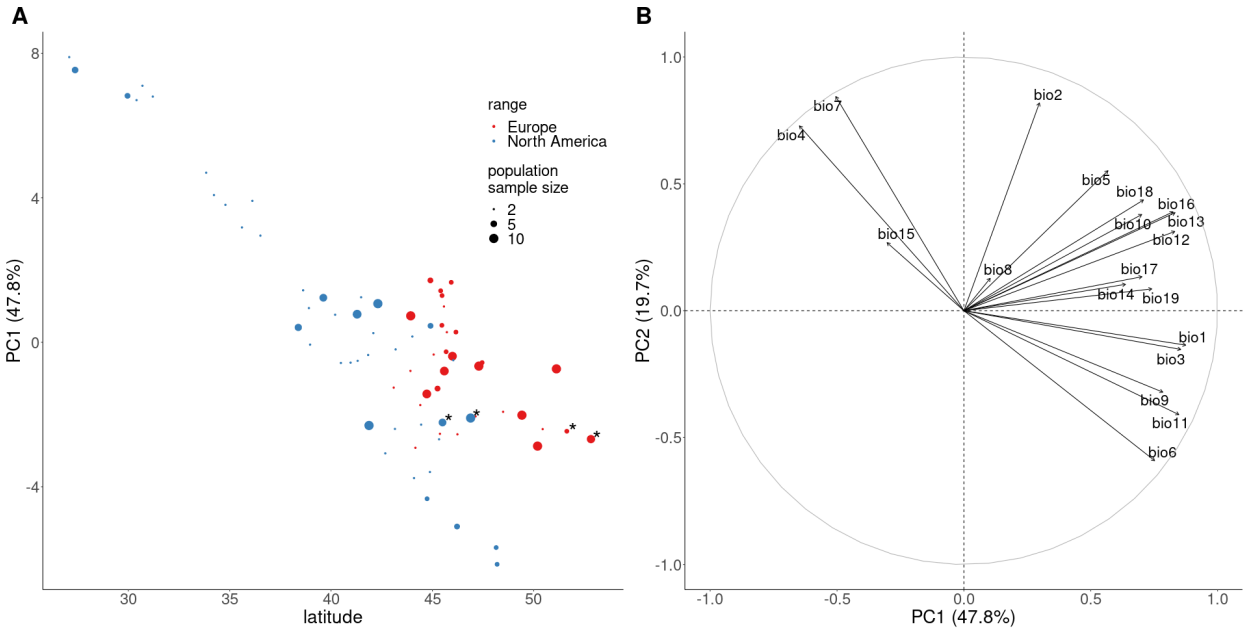

Figure S3. Environmental comparison of North American and European *A. artemisiifolia* ranges. A. The first principle component of 19 bioclimatic variables against latitude for modern ragweed populations in North America (red) and Europe (blue), with asterisks identifying populations with high *ELF3* allele frequencies. **B**. A variable correlation plot for 19 bioclimatic variables.

Figure S4. An example herbarium specimen of *Ambrosia artemisiifolia* (left) and a detail (right) showing the mature male inflorescence (solid line) and seeds (dashed lines).

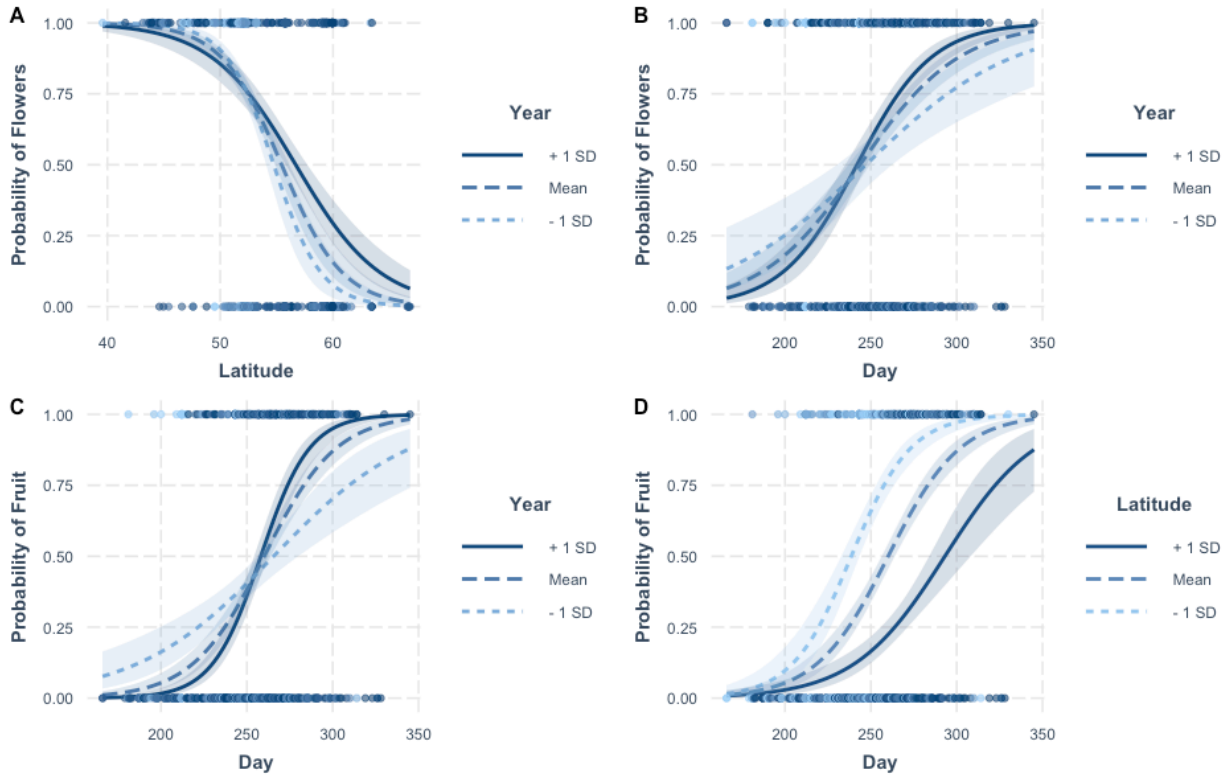

Figure S5. Interaction plots illustrating the results of generalized linear models examining the presence of mature male inflorescences (probability of flowers) or mature fruit (probability of fruit) in herbarium specimens of *A. artemisiifolia* in Europe as a function of collection day (Day), latitude of origin (Latitude) and collection year (Year). The predicted probability of observing flowers is plotted as a function of latitude (**A**), or collection day (**B**) for different collection years (mean collection year +/- 1 SD). The predicted probability of observing fruit is plotted against collection day for different collection years (mean collection year +/- 1 SD; **C**) or latitudes (mean collection latitude +/- 1 SD; **D**). Confidence intervals for the predictions are shown as are the raw data.

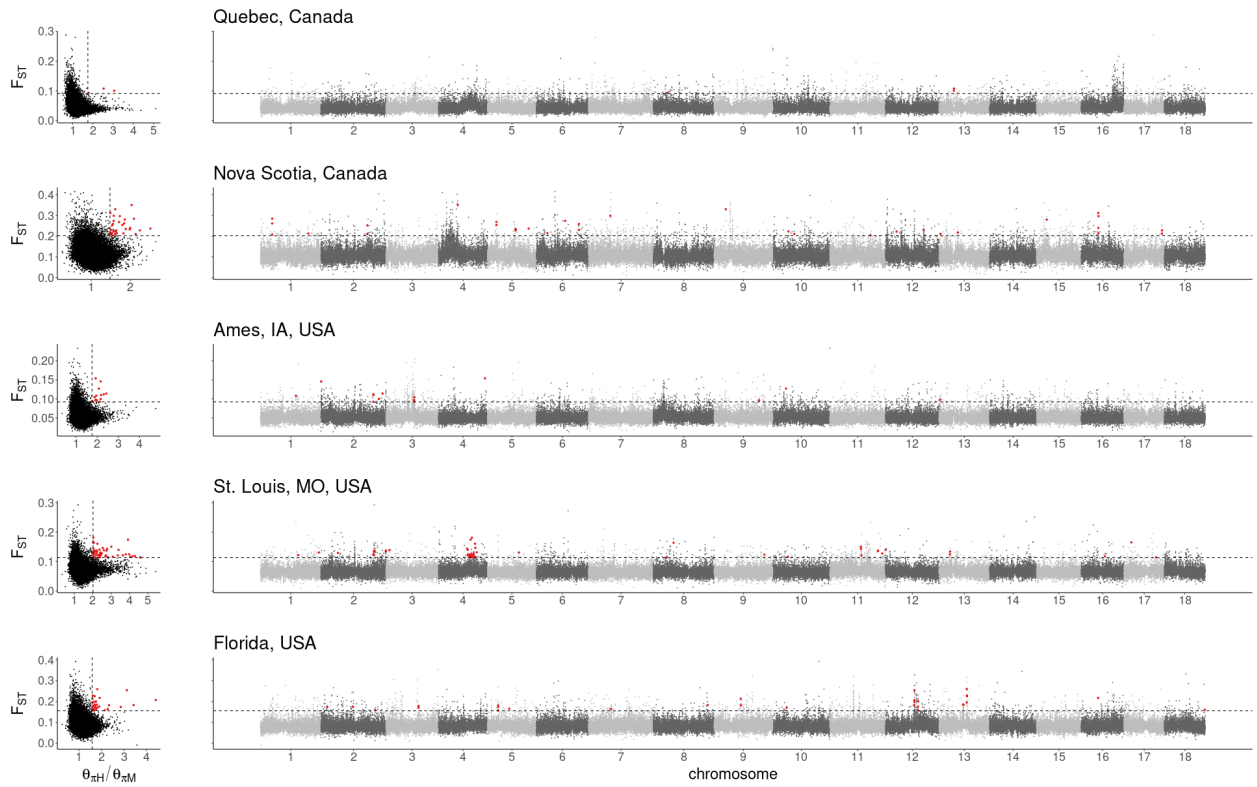

Figure S6. Distributions of F_{ST} and $\theta_{\pi H}/\theta_{\pi M}$ between historic and modern samples from North American populations, and F_{ST} against genomic location. Red points indicate putative selective sweep windows, which are in top one percent of per-window F_{ST} and $\theta_{\pi H}/\theta_{\pi M}$ (dashed lines).

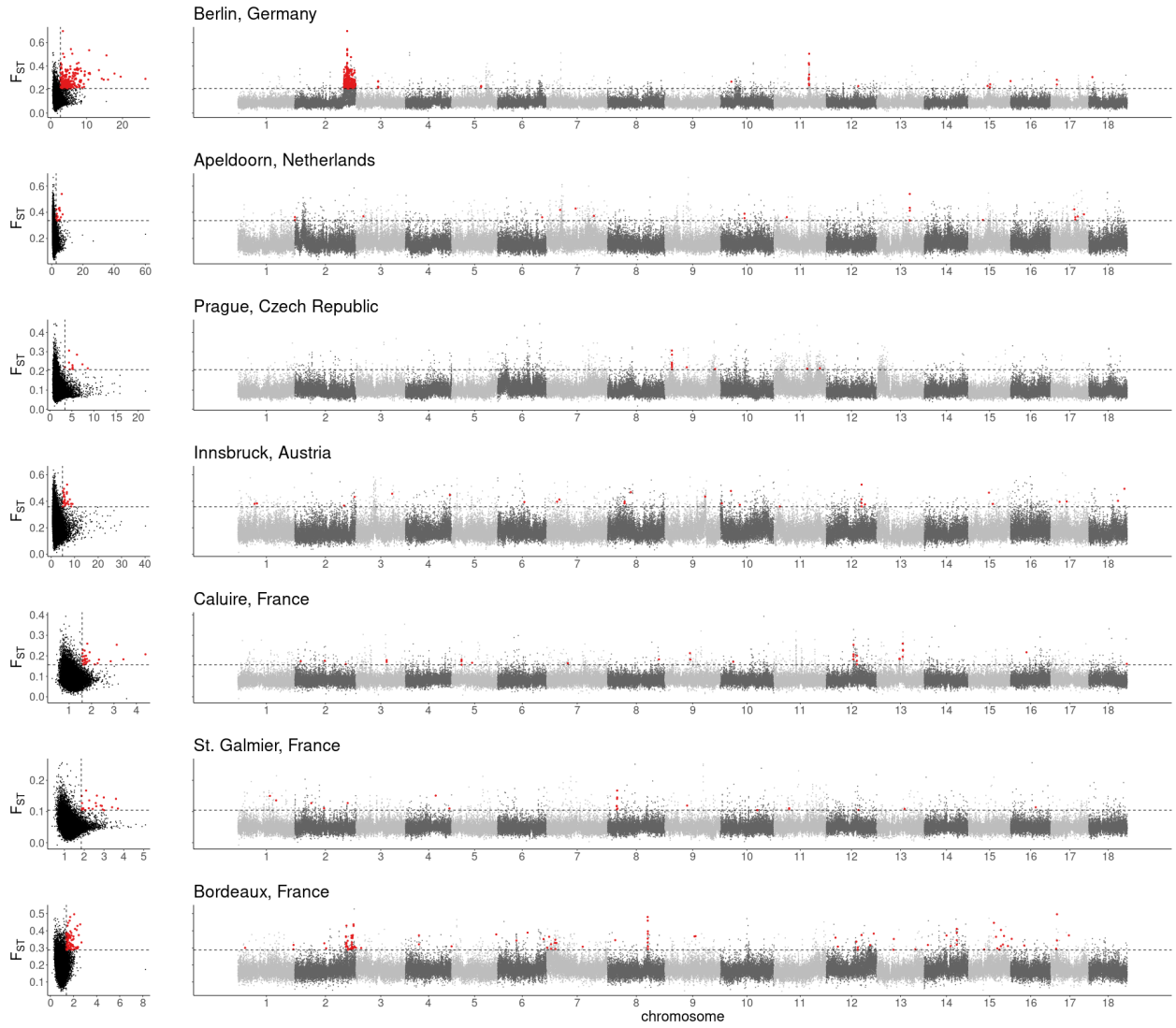

Figure S7. Distributions of F_{ST} and $\theta_{\pi H}/\theta_{\pi M}$ between historic and modern samples from European populations, and F_{ST} against genomic location. Red points indicate putative selective sweep windows, which are in top one percent of per-window F_{ST} and $\theta_{\pi H}/\theta_{\pi M}$ (dashed lines).

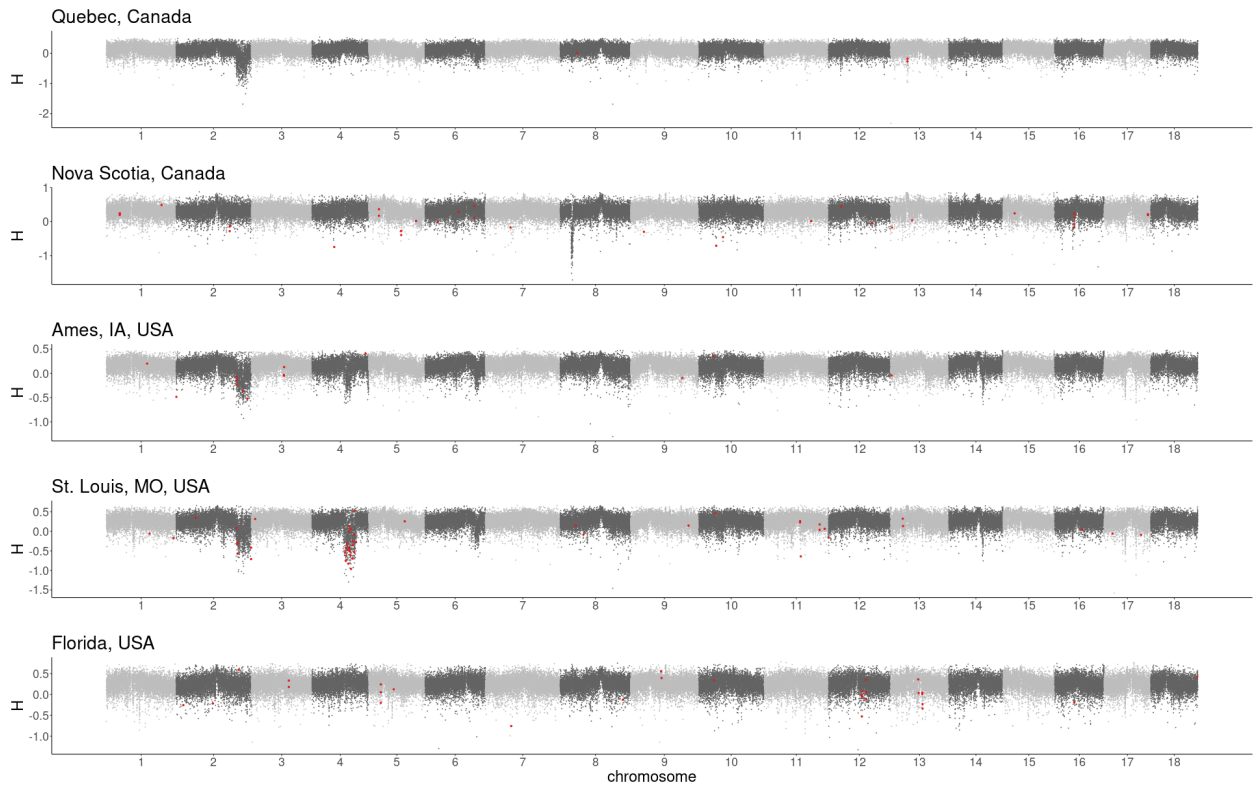

Figure S8. Fay and Wu's *H* against genomic location for modern North American populations. Red points indicate putative selective sweep windows from historic-modern comparisons.

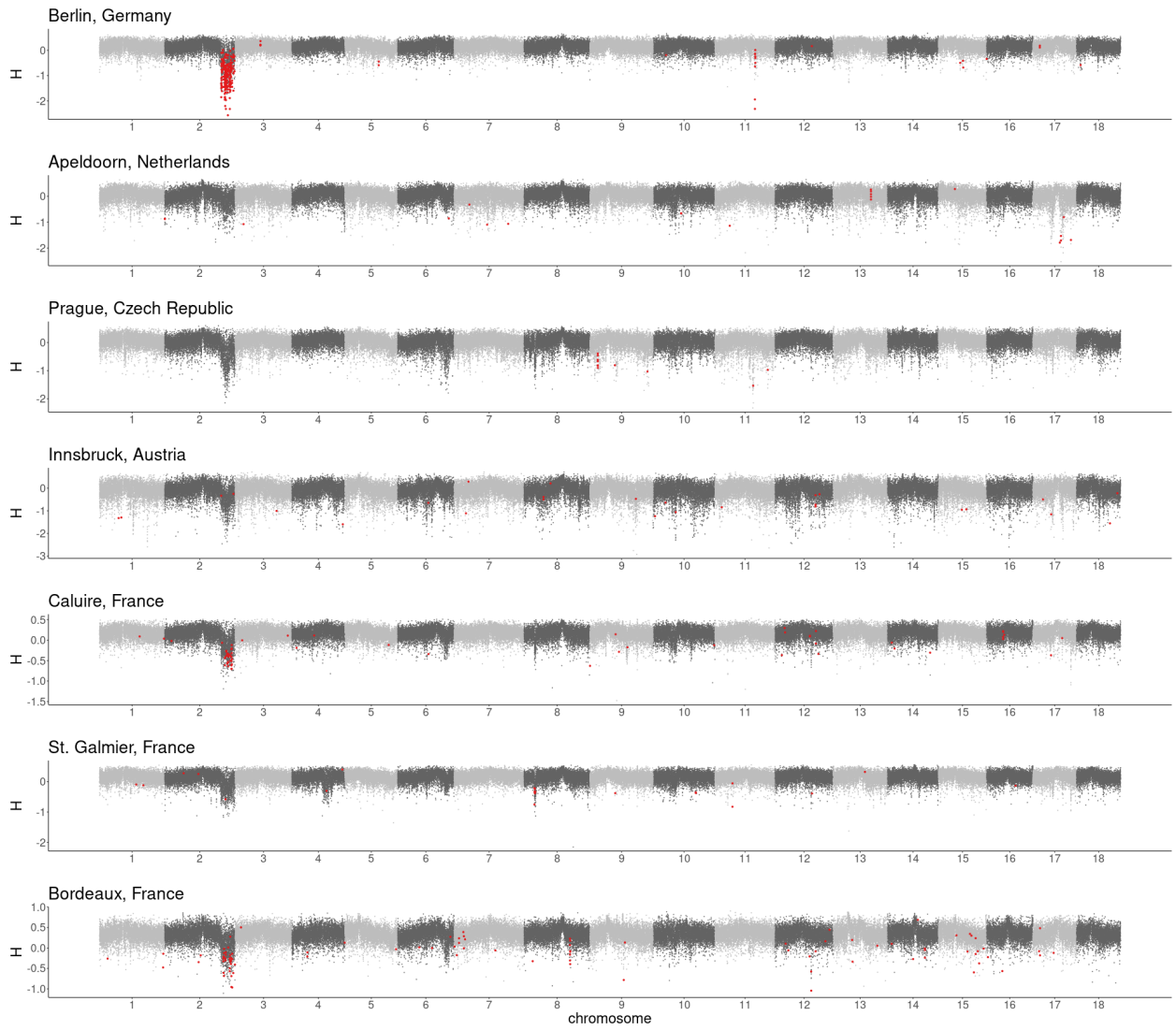

Figure S9. Fay and Wu's *H* against genomic location for modern European populations. Red points indicate putative selective sweep windows from historic-modern comparisons.

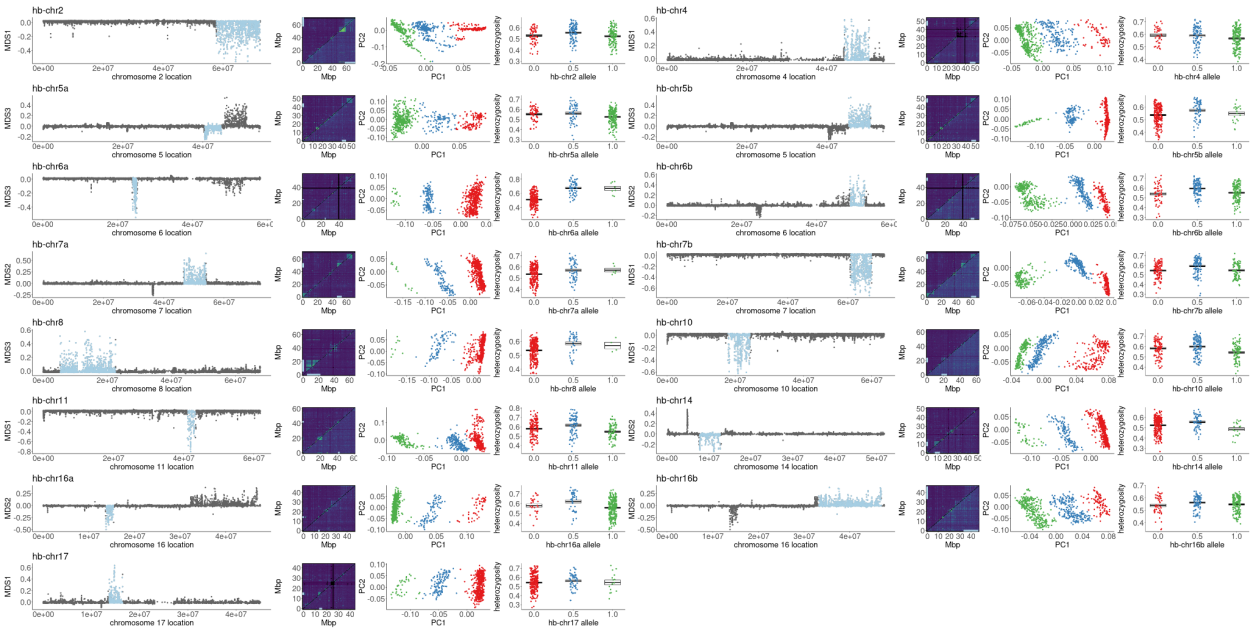

Figure S10. Haploblocks display extreme, divergent, local population structure (pale blue regions; first column). Haploblock regions (indicated by pale blue lines; second column) correspond to blocks of linkage disequilibrium (second highest r^2 in 0.5Mb windows) apparent using all modern samples (top triangle) but often reduced or absent using only samples homozygous for the more common haploblock genotype (bottom triangle). Haploblock genotypes were assigned by kmeans clustering (colours; third column) using the first two principal components of genetic variation across haploblock regions. Heterozygous haploblock genotypes show elevated mean per-site heterozygosity (fourth column; boxes denote mean and SEM).

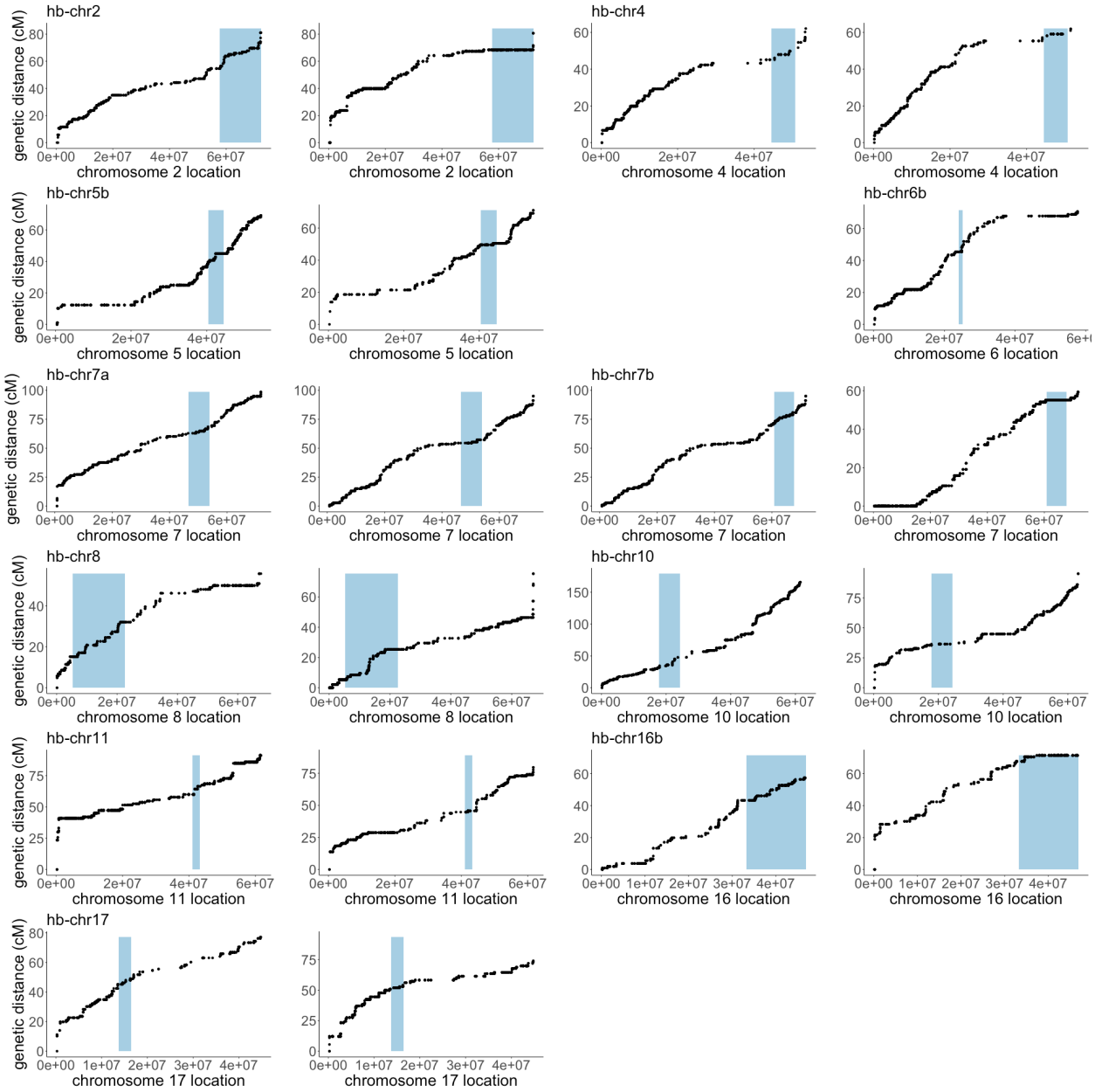

Figure S11. Evidence of genotype-specific reductions in recombination in haploblock regions. Genetic distance (cM) against physical distance (bp) along a portion of each scaffold is shown. Haploblock regions are shown in pale blue. Example maps are displayed showing both low recombination rates (left) and high recombination rates (right) for each haploblock.

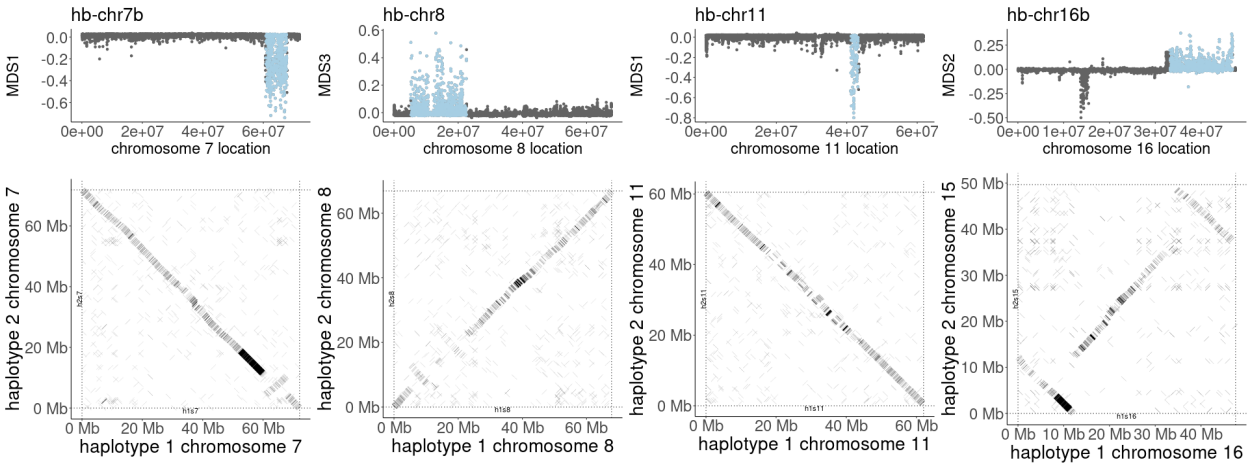

Figure S12. Population-genomic signatures of inversions (top row; from fig. S9) that correspond to inversion polymorphisms segregating in our diploid reference genome (bottom row; from fig. 1B).

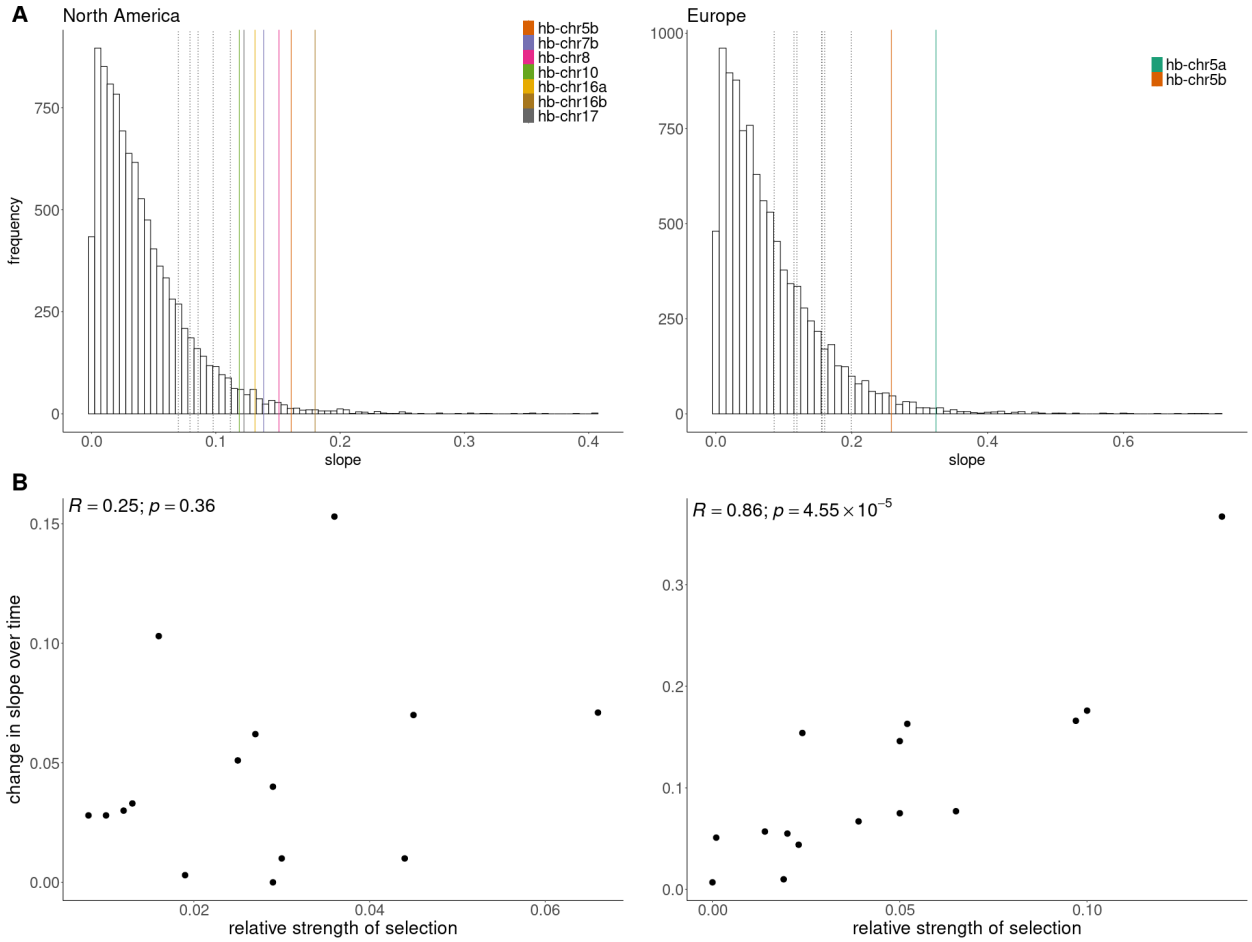

Figure S13. A. The distribution of slope estimates from generalized linear models of population allele counts against latitude for 10,000 randomly selected SNPs in each range. The vertical lines show the slope estimates for haploblocks with statistical associations with latitude in one range (table S12). Solid lines represent estimates in the 5% tail of each distribution while dotted lines fall below that cut-off. **B.** The change in the slope of the relationship between latitude and haplotype frequency (see table S15) between historic and modern samples compared to the estimate of selection along the latitudinal cline for the 15 haploblocks (estimated from modern data in each range). A strong relationship was detected in the invasive European, but not the native North American range.

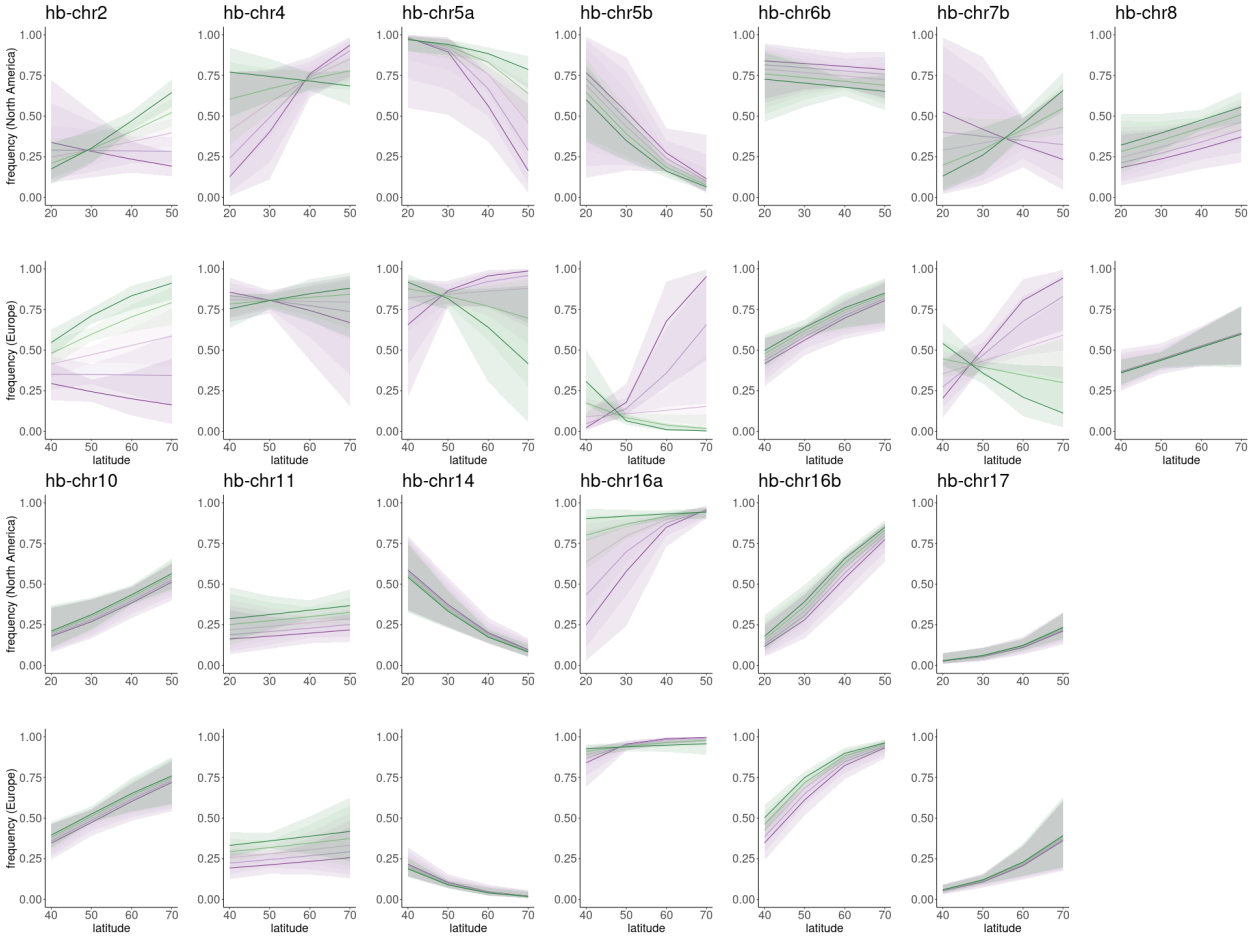

Figure S14. Logistic regression models with 95% CI ribbons (see table S12-S17 for model details) of haploblock frequency (allele 1) against latitude for each haploblock that shows a significant latitude, time or range effect, or significant interactions between these effects, across five time bins ranging from most historic (purple) to most modern (green).

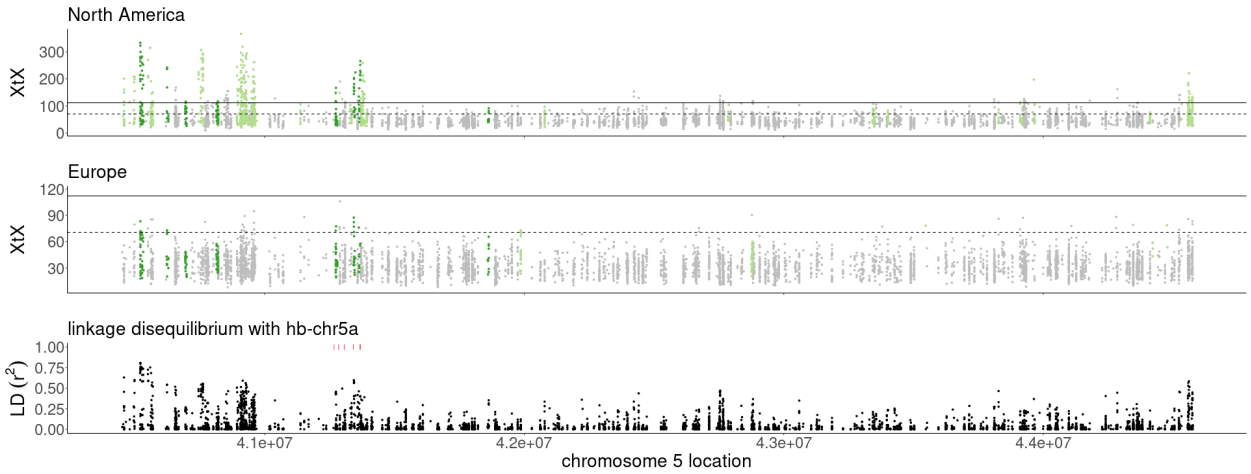

Figure S15. A detailed analysis of the hb-chr5 region (5:40446189-44576095). XtX and XtX-EAA outlier windows zoomed from fig. 2C, and linkage disequilibrium (r^2) between SNPs in the region and hb-chr5a haploblock genotype. A cluster of six pectate lyase genes, consisting of the top BLAST hit for *Amba1* and closely-related paralogues, are indicated in red above the linkage disequilibrium plot.

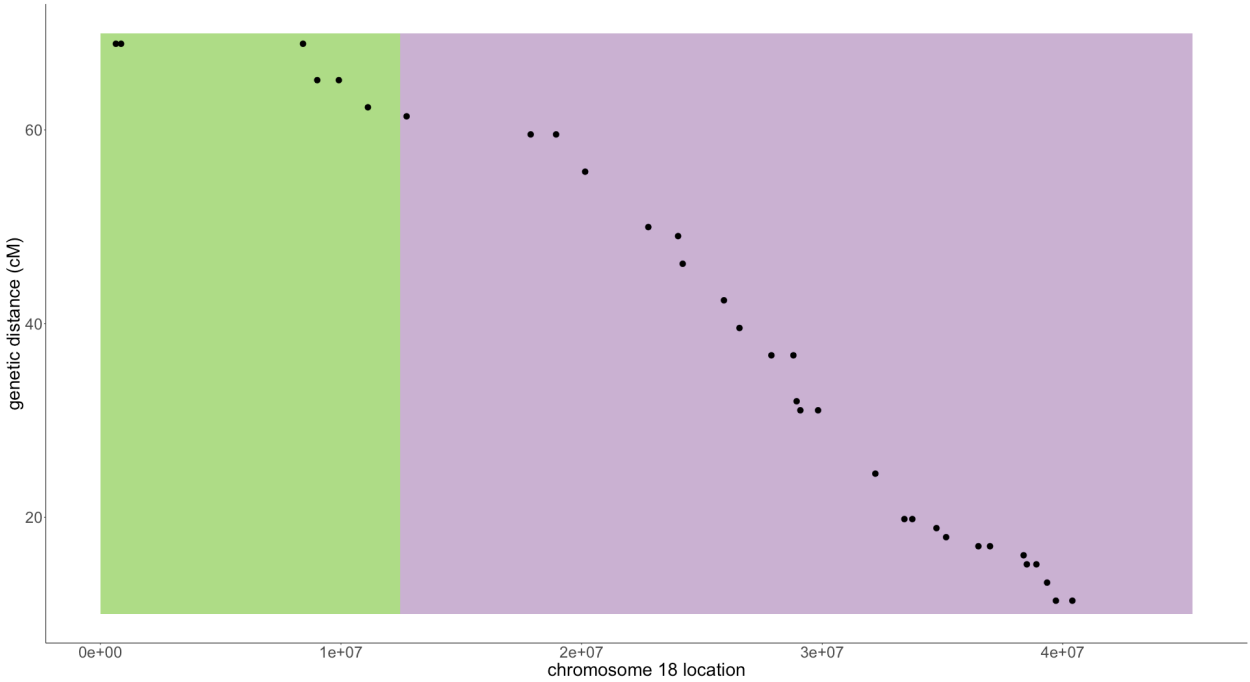

Figure S16. Genetic markers support the combination of two scaffolds (green and purple) to assemble haplotype 1 chromosome 18.

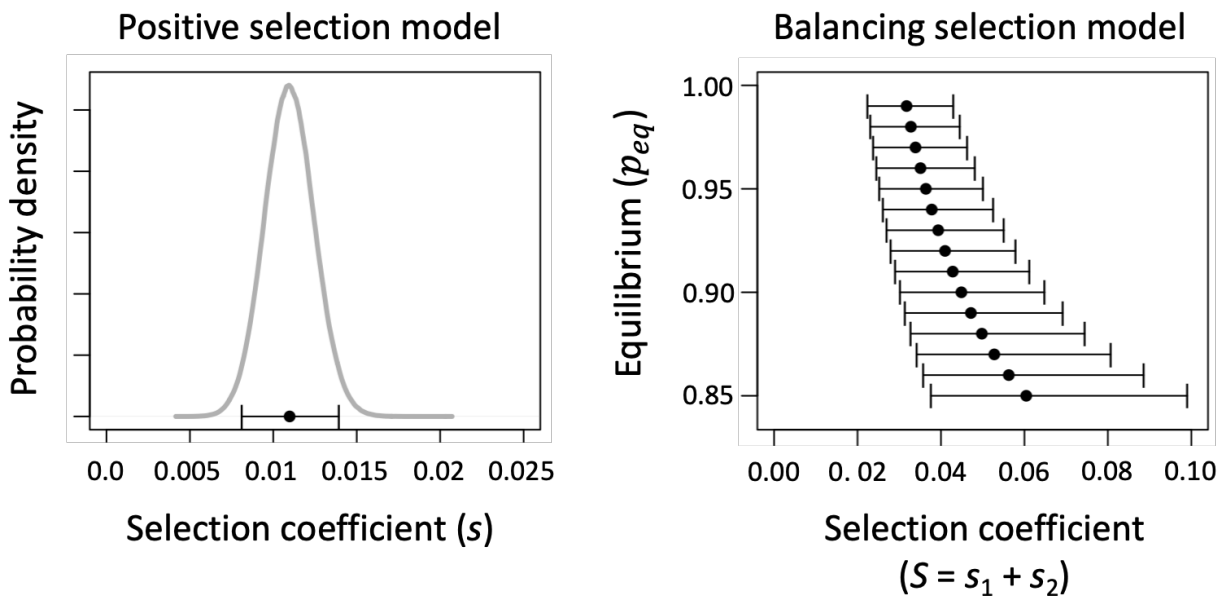

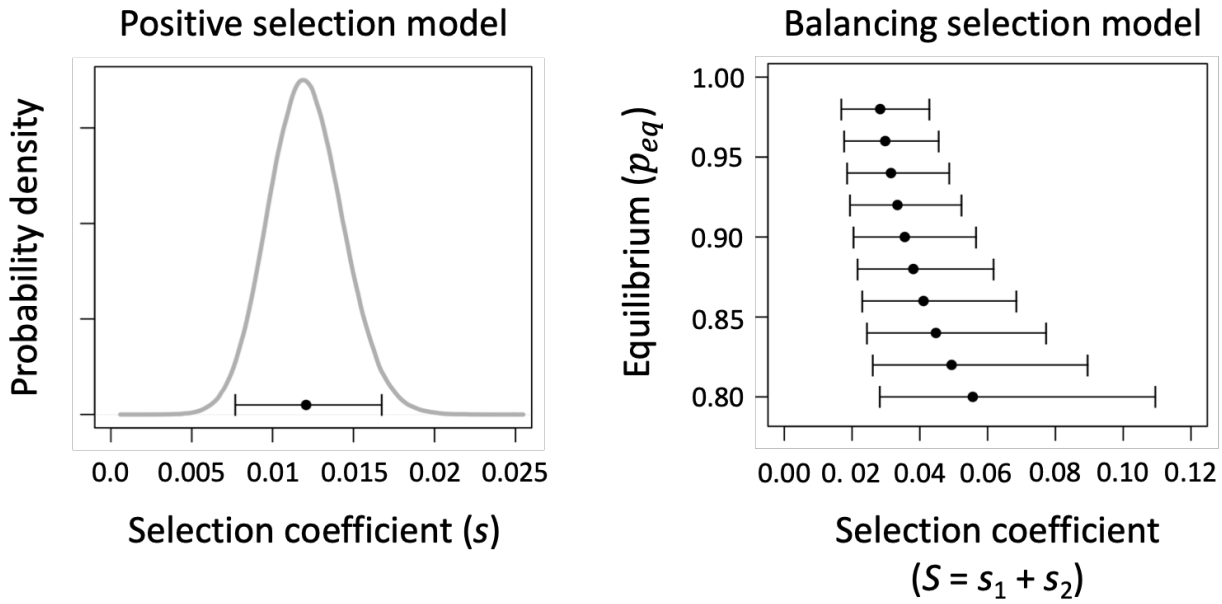

Figure S17. Selection coefficients consistent with observed frequency changes of the hb-chr2 haplotype, under models of positive selection (left) and balancing selection (right). The left-hand panel shows the distribution of *s* values (gray) and the 95% CI for *s* (in black: parallel to the *x*-axis), consistent with temporal change in the hb-chr2 haploblock. The distribution of s is based on simulations of 10^6 initial and final frequencies of the haploblock that are consistent with the estimated frequencies and error in the estimates. Eq. (S1) was used to calculate a value of *s* for each set of initial and final frequencies during the time interval between 1902 (the median year of historic samples used in this analysis) and 2014 (contemporary). The right-hand panel shows the selection coefficients under the balancing selection model that are consistent with observed

1005 changes in hb-chr2 inversion frequencies in Europe. Across the range of possible polymorphic
1006 equilibrium frequencies under balancing selection, equilibria near unity (*e.g.*, p_{eq} = 0.98) require
1007 modestly strong selection (average *S* = 0.028; 95% CI = [0.017, 0.043]) to explain the observed
1008 frequency changes in hb-chr2, and lower equilibrium states require stronger selection.

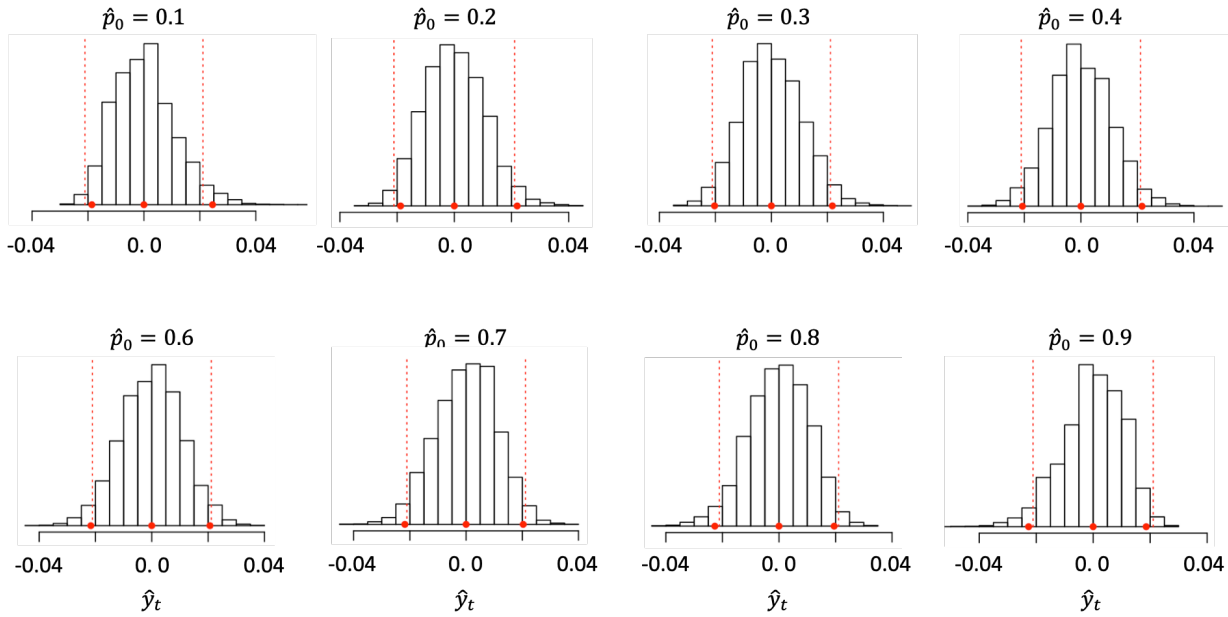

Figure S18. Simulated distribution of the scaled metric of divergence, $\hat{y}_t$, given different estimated values of the initial (historic) allele frequency. Each distribution is based on 10^4 independent and neutrally evolving SNPs. The simulations use n_0 = 182, n_t = 312, and t = 131, with a moderate effective population size (N_e = 10^4). Histograms show the distribution of $\hat{y}_t$ estimates, the red circles show the simulated mean and 95% confidence intervals for simulated data, and the vertical broken red lines show +/- 1.96 SD, where SD is the square root of our analytical expression for $var[\hat{y}_t]$.

SUPPLEMENTARY TEXT

S1: Estimating the strength of selection on hb-chr2 using temporal changes

The putative inversion hb-chr2 increases in frequency between historical and contemporary European populations, consistent with selection favouring its increase in the invasive range. To infer strengths of selection that are sufficient to explain the pattern of frequency change, we considered two simple, deterministic models of selection for the inversion:

- A *positive selection model* in which the inversion is favoured over the standard haplotype and is eventually expected to fix in European populations
- A *balancing selection model* in which the increased frequency of the inversion brings it closer to a hypothetical polymorphic equilibrium within the European range.

We note that, while genetic drift will inevitably play some role in the allele frequency dynamics of loci subject to selection (because populations are finite in size), evolutionary dynamics are well-approximated by deterministic models provided the allele frequencies of favourable variants are at least moderately common in the population and selection is strong relative to the inverse of the effective population size[81]. Both assumptions are easily met, and should apply to the hb-chr2 haplotype.

Positive selection model

Let p represent the frequency of the hb-chr2 inversion haplotype. Under a model of positive selection with no dominance, the general solution for the ratio of inversion to standard haplotype frequencies (the ratio defined as $x = p/(1 - p)$) is:

$$x_t = x_0(1 + s)^t$$

which is easily rearranged to solve for the frequency of the inversion:

$$p_t = \frac{p_0(1 + s)^t}{1 - p_0 + p_0(1 + s)^t}$$

(*e.g.* [82] pp. 200-203), where s is the fitness increase associated with each copy of the inversion (*i.e.*, the fitnesses of inversion heterozygotes and homozygotes, relative to individuals without the inversion, are $1 + s$ and $(1 + s)^2$, respectively). Under this parameterization, the difference in

relative fitness between inversion and standard haplotype homozygotes is $2s(1 + s/2) \sim 2s$, with the $2s$ approximation applying when s is small (as we infer below).

The strength of selection is a function of the inversion frequency shift from p_0 to p_t following t generations of evolution:

$$s = exp\left[\frac{1}{t} log\left(\frac{p_t(1-p_0)}{p_0(1-p_t)}\right)\right] - 1 \quad (1)$$

Since common ragweed is an annual plant, t refers to the number of years that have transpired, and p_0 and p_t can be estimated (with uncertainty) from the contemporary and historical samples.

We used eq. (1) to infer strengths of selection (s) that would be consistent with the estimated change in inversion frequencies over time, focusing on the estimated frequencies at the midpoint of the European range (table S20). Inversion frequencies were estimated as p = 0.37 (95% CI = {0.30, 0.45}) in the historic samples, with 1902 representing the median date of samples included in the analysis. For modern samples (sampling date of 2014), the estimated frequency was p = 0.69 (95% CI = {0.60, 0.76}). Given the large sizes of historic and modern collections, and the fact that haploblock frequencies remain intermediate across time, the distance between the 95% CI bounds will be roughly 3.92 standard errors of each frequency estimate. To take into account uncertainty in the frequency estimates, we simulated values of p_t (modern) and p_0 (historic) and used these values, along with eq. (1), to generate a distribution of selection coefficients (s) consistent with our data. Specifically, for a given time interval (i.e., historic or modern), we drew 10^6 pseudo-random numbers from a normal distribution with mean corresponding to the point estimate of the haplotype frequency for the interval (i.e., 0.37 for historic; 0.69 for modern), and a standard deviation of $d/3.92$, where d is the difference between the 95% CI of the estimate. Our analysis yielded 10^6 values of s that were compatible with the set of simulated inversion frequencies. The estimate and 95% confidence interval for s was calculated directly from the distribution of s values.

Balancing selection model

Although temporal changes in the hb-chr2 haplotype are consistent with changes predicted under the positive selection model presented above, we wished to also evaluate an alternative

model in which balancing selection favours evolution of the inversion towards an equilibrium polymorphic state. To explore the strength of selection towards a hypothetical equilibrium within the European range, we considered a simple model of overdominant selection. Note that the overdominant selection model is dynamically equivalent to many other balancing selection models provided the differences in fitness among genotypes are small (consistent with our analysis below). Our results based on the overdominance model should, therefore, apply more broadly to other scenarios of balancing selection, including scenarios involving negative frequency-dependence and antagonistic pleiotropy[83,84].

Following standard theory (*e.g.*, [85] pp. 270-272), the expected change in frequency over a generation (generation t to generation $t + 1$) is:

$$\Delta p_t = p_{t+1} - p_t = \frac{(s_1 + s_2)p_t(1 - p_t)(p_{eq} - p_t)}{1 - p_{eq}(1 - p_{eq})(s_1 + s_2) - (p_t - p_{eq})^2(s_1 + s_2)}$$

where s_1 and s_2 refer to the fitness costs of being homozygous for inversion and standard haplotypes, respectively, and p_{eq} is the equilibrium frequency of the inversion. Using a continuous-time approximation, we can solve for the overall selection coefficient, $S = s_1 + s_2$, that is consistent with a frequency shift from p_0 to $p_t < p_{eq}$ across t generations:

$$t = \int_{p_0}^{p_t} \frac{1 - Sp_{eq}(1 - p_{eq}) - S(x - p_{eq})^2}{Sx(1 - x)(p_{eq} - x)} dx$$

$$= \frac{\left(p_{eq} - Sp_{eq}(1 - p_{eq})\right) log\left(\frac{1 - p_t}{1 - p_0}\right) + (1 - p_{eq})(1 - Sp_{eq}) log\left(\frac{p_t}{p_0}\right) - \left(1 - Sp_{eq}(1 - p_{eq})\right) log\left(\frac{p_t - p_{eq}}{p_0 - p_{eq}}\right)}{Sp_{eq}(1 - p_{eq})}$$

Solving for S, gives us:

$$S = \frac{p_{eq}\ log\left(\frac{1 - p_t}{1 - p_0}\right) + (1 - p_{eq}) log\left(\frac{p_t}{p_0}\right) - log\left(\frac{p_{eq} - p_t}{p_{eq} - p_0}\right)}{p_{eq}(1 - p_{eq})\left(t + log\left(\frac{1 - p_t}{1 - p_0}\right) + log\left(\frac{p_t}{p_0}\right) - log\left(\frac{p_{eq} - p_t}{p_{eq} - p_0}\right)\right)} \quad (2)$$

To infer the strength of selection (*S*) that would be consistent with observed inversion frequencies and a given equilibrium value (p_{eq}), we simulated 10^6 inversion frequencies consistent with the estimated frequency and its sample size at historical time point (~1902) and 10^6 frequencies consistent with the estimate for the contemporary sample. (Frequencies were simulated as described in the positive selection model section, above). We used each pair of simulated inversion frequencies and eq. (2) to infer the value of *S* consistent with the frequency values. The resulting distribution of 10^6 simulated *S* values was used to calculate 95% CI for *S* consistent with the data. We focused on equilibrium values outside of the 95% CI for contemporary inversion frequencies (*i.e.*, values of p_{eq} between 0.80 and 1). The results show that plausible selection coefficients under scenarios of balancing selection are consistently greater than those of the positive selection model (fig. S17). Selection under the positive selection model can, therefore, be regarded as a lower bound for the strength of selection consistent with the observed temporal changes in European hb-chr2 inversion frequencies.

S2: Selection estimated from spatial changes in haploblock frequency

Cline theory

We will consider the simplest possible population genetics model of local adaptation in a species that is continuously distributed along a single axis of space (*e.g.*, from north to south), with *x* representing location along the axis, and *x* = 0 representing a specific point in space where the environment relevant to selection at a focal locus—in this instance, a genomic region segregating for an inversion—changes abruptly. We assume that the inversion is favoured in locations where *x* > 0 (*e.g.*, in the north) and the standard haplotype is favoured in locations where *x* < 0 (*e.g.*, the south). We further assume that population density is uniform across the spatial gradient (at least within the vicinity of the environmental transition), and that individual dispersal follows a symmetric, Gaussian distribution with variance of σ^2 (the unit of distance is arbitrary, though σ and *x* should have the same units, *e.g.*: if distance in *x* is measured in kilometres then σ should also be expressed in km; σ^2 corresponds to the migration rate, *m*, between adjacent patches in discrete stepping stone models)[86].

Given the stated assumptions, the inversion frequency dynamics at location *x* can be described using the following reaction diffusion equation:

$$\frac{dp(x)}{dt} = \frac{\sigma^2}{2}\frac{d^2p(x)}{dx^2} + \Delta p_{sel}(x)$$

where $\Delta p_{sel}(x)$ is the local response to selection[44,87]. With symmetrical strengths of selection at each side of the environmental transition, and no dominance, then $\Delta p_{sel}(x) \approx sp(x)\big(1 - p(x)\big)$ within the northern region of the range where the inversion is favoured, and $\Delta p_{sel}(x) \approx -sp(x)\big(1 - p(x)\big)$ in the southern portion of the range where the standard haplotype is favoured; both expressions are valid for modest-to-weak selection (0 < *s* < ~0.1). As in the positive selection model presented above, this parameterization leads to local fitness differences of ~2*s* between inversion and standard haplotypes. Incorporating dominance does not change our results provided the dominance relations between the alleles are consistent across the range (*i.e.*, under "parallel dominance"[88]). At equilibrium between selection and migration, the maximum cline slope will be:

$$\frac{dp(x)}{dx} = \sqrt{\frac{s}{3\sigma^2}} \tag{3}$$

Following Roughgarden[87], the equilibrium general solution for the cline is:

$$p(x) = -\frac{1}{2} + \frac{3}{2}\left[tanh\left(x\sqrt{\frac{s}{2\sigma^2}} + \left(\sqrt{\frac{2}{3}}\right)\right)\right]^2 \; for\; x > 0$$

$$p(x) = \frac{3}{2} - \frac{3}{2}\left[tanh\left(-x\sqrt{\frac{s}{2\sigma^2}} + \left(\sqrt{\frac{2}{3}}\right)\right)\right]^2 \; for\; x < 0$$

Estimating cline slopes by logistic regression

A logistic regression model for inversion frequency as a function of geographic location (*x*) is:

$$f(x) = \frac{1}{1 + e^{-(\beta_0 + \beta_1 x)}}$$

The parameters of the model (β_0 and β_1) can be estimated by fitting the data to the log-odds (logit):

$$log\left(\frac{f(x)}{1 - f(x)}\right) = \beta_0 + \beta_1 x$$

Using the theoretical cline functions (above) to calculate the log-odds, we obtain the following slopes. For shallow clines—those with a geographically broad clinal region, where the maximum slope can be accurately estimated—we have:

$$\frac{d\; log\left(\frac{p(x)}{1 - p(x)}\right)}{dx} = 4\sqrt{\frac{s}{3\sigma^2}}$$

For steep clines—those with a narrow clinal region, where the maximum slope will be underestimated using the logit function—we have:

$$\frac{d\ log\left(\frac{p(x)}{1-p(x)}\right)}{dx} = \sqrt{\frac{2s}{\sigma^2}}$$

We get the following estimates from these two limits:

$$\frac{\sqrt{3}\beta_1}{4} \leq \frac{\sqrt{s}}{\sigma} \leq \frac{\beta_1}{\sqrt{2}}$$

Given the point estimates and 95% CI for β_1 in table S16, we can calculate plausible ranges for the lower bound of $\frac{\sqrt{s}}{\sigma}$ by multiplying the values for β_1 by $\frac{\sqrt{3}}{4}$

Comparisons of spatially varying selection among haploblocks

All of these estimates rely on the assumption that the system is at equilibrium within each range and time point, though that assumption may be more valid for some cases then others. To the extent that it is a reasonable assumption, and if effects of gene flow are consistent across the genome, we can estimate the relative strength of spatially varying selection on different haploblocks (e.g., haploblocks arbitrarily labeled “A” and “B”) as:

$$\frac{s_A}{s_B} = \left(\frac{\beta_{1,A}}{\beta_{1,B}}\right)^2$$

S3: A simple null model of temporal allele frequency changes under drift

To evaluate whether temporal changes in candidate loci exceeded neutral expectations under drift in the absence of selection, we compared the distribution of the following standardized measure of divergence for a large sample of putatively neutral SNPs with the same metric calculated for selection candidates. Let divergence after *t* generations be defined as:

$$y_t = \frac{p_t - p_0}{\sqrt{tp_0(1-p_0)}}$$

where p_0 and p_t represent the initial and final frequencies of an allele at a bi-allelic locus. We shall show below that, provided loci with low minor allele frequencies are first filtered out of the analysis, the metric follows a symmetric distribution that is approximately independent of the initial frequency.

For a locus with initial frequency of p_0, the frequency after one generation of drift is given by:

$$p_1 = \frac{x}{2N_e}$$

where x is a random variable drawn from a binomial distribution with parameters $2N_e$ and p_0, where N_e is the effective population size (which follows the standard, Wright-Fisher model of genetic drift). The expected value and the variance for p_1 is therefore p_0 and $p_0(1 - p_0)/2N_e$, respectively. The model can be extrapolated for a modest number of generations, after which the allele frequency (p_t after t generations) has an expected value of p_0 and variance of $tp_0(1 - p_0)/2N_e$. The latter will eventually break down as t increases, but it should be appropriate provided $t/2N_e$ is small and the initial frequency is not too close to zero or one, as we assume below. From these expressions, the standardized measure of allele frequency divergence in the population under drift (and no selection) has an expectation of zero and a variance of:

$$var(y_t) = \frac{var(p_t)}{tp_0(1-p_0)} = \frac{1}{2N_e}$$

which is independent of the initial frequency.

In reality, error in the estimates of p_0 and p_t will also affect the test statistic, and this will tend to inflate the variance, but doesn't alter the conclusion that (under a null model of drift with no selection) the distribution of the estimates of y_t (which we denote as $\hat{y}_t$) will be roughly independent of the initial allele frequencies in the historic sample. If we define $\hat{p}_t$ and $\hat{p}_0$ is the estimates of the allele frequencies, then our test statistic is:

$$\hat{y}_t = \frac{\hat{p}_t - \hat{p}_0}{\sqrt{t\hat{p}_0(1-\hat{p}_0)}}$$

The mean and variance of $\hat{y}_t$ can be calculated using the following steps:

Step 1. The expected value and variance of $\hat{p}_t$ conditioned on the final population frequency (*i.e.*, the true frequency, p_t) is:

$$E[\hat{p}_t|p_t] = p_t$$

$$var[\hat{p}_t|p_t] = \frac{p_t(1-p_t)}{n_t}$$

where n_t represents the number of genes sampled in the contemporary population (*e.g.*, for hb-chr2, 156 individuals were sampled for the contemporary estimate in Europe; given diploidy, we have n_t = 312).

Step 2. The expected value and variance of $\hat{p}_t$ conditioned on the initial population frequency (*i.e.*, the true frequency, p_0) is:

$$E[\hat{p}_t|p_0] = E([\hat{p}_t|p_t]\,|p_0) = E(p_t|p_0) = p_0$$

$$var[\hat{p}_t|p_0] = E(var[\hat{p}_t|p_t]\,|p_0) + var([\hat{p}_t|p_t]\,|p_0) = E\left(\frac{p_t(1-p_t)}{n_t}|p_0\right) + var(p_t|p_0)$$

$$var[\hat{p}_t|p_0] = \frac{E(p_t|p_0)\,(1-E(p_t|p_0)\,) - var(p_t|p_0)}{n_t} + var(p_t|p_0) = \frac{p_0(1-p_0)}{n_t} + \frac{tp_0(1-p_0)}{2N_e}\left(1-\frac{1}{n_t}\right)$$

where N_e is the effective population size, and n_0 is the number of genes sampled in the historic population.

Step 3. Among loci with an initial frequency estimate of $\hat{p}_0$, the true initial frequency (p_0) will, roughly, follow a distribution with mean and variance of $\hat{p}_0$ and $\hat{p}_0(1-\hat{p}_0)n_0^{-1}$, respectively. Consequently, the expected value and the variance of $\hat{p}_t$ conditioned on the initial frequency estimate $\hat{p}_0$ will be:

$$E[\hat{p}_t|\hat{p}_0] = E\{[\hat{p}_t|p_0]\,|\hat{p}_0\} = E\{p_0|\hat{p}_0\} = \hat{p}_0$$

$$var[\hat{p}_t|\hat{p}_0] = E\{var[\hat{p}_t|p_0]\,|\hat{p}_0\} + var\{E[\hat{p}_t|p_0]\,|\hat{p}_0\} = E\left\{\frac{p_0(1-p_0)}{n_t} + \frac{p_0(1-p_0)}{2N_e}t\left(1-\frac{1}{n_t}\right)|\hat{p}_0\right\} + var\{p_0\,|\hat{p}_0\}$$

$$var[\hat{p}_t|\hat{p}_0] = \hat{p}_0(1-\hat{p}_0)\left[\frac{1}{n_t} + \frac{1}{2N_e}t\left(1-\frac{1}{n_t}\right)\right]\left(1-\frac{1}{n_0}\right) + \frac{\hat{p}_0(1-\hat{p}_0)}{n_0}$$

Therefore, the expected value and the variance for $\hat{y}_t$, given an initial frequency estimate of $\hat{p}_0$, will be:

$$E[\hat{y}_t|\hat{p}_0] = E\left[\frac{\hat{p}_t - \hat{p}_0}{\sqrt{t\hat{p}_0(1-\hat{p}_0)}}|\hat{p}_0\right] = 0$$

$$var[\hat{y}_t|\hat{p}_0] = \frac{var[\hat{p}_t|\hat{p}_0]}{t\hat{p}_0(1-\hat{p}_0)} = \frac{\left[\frac{1}{n_t} + \frac{1}{2N_e}t\left(1-\frac{1}{n_t}\right)\right]\left(1-\frac{1}{n_0}\right) + \frac{1}{n_0}}{t}$$

Note that the final expressions are, once again, independent of the initial frequency, though (once again) the pathway to these results requires that $\hat{p}_0$ is not too close to zero or one. Because of this independence, we can pool loci with different initial frequency estimates (with pooling after loci with low minor allele frequency are first removed) to approximate the null distribution for $\hat{y}_t$ as well as the variance of the test statistic: $var[\hat{y}_t] = var[\hat{y}_t|\hat{p}_0]$.

Incidentally, the expression for $var[\hat{y}_t|\hat{p}_0]$ can be rearranged by solving for the effective population size across the *t* generations, *i.e.*:

$$N_e = \frac{\frac{1}{2}t\left(1-\frac{1}{n_t}\right)\left(1-\frac{1}{n_0}\right)}{tvar[\hat{y}_t] - \frac{1}{n_0} - \frac{1}{n_t}\left(1-\frac{1}{n_0}\right)}$$

A rough estimate of N_e can be obtained from a set of independent neutral SNPs by using the above formula with the estimated variance of $\hat{y}_t$ substituted for $var[\hat{y}_t]$.

Simulations

We carried out simulations to test the theoretical predictions of the neutral model presented above, and found that they work well as long as the initial allele frequency estimates are not too close to zero or one ($0.1 < \hat{p}_0 < 0.9$ performs well and $0.2 < \hat{p}_0 < 0.8$ is excellent). Simulations for a given value of $\hat{p}_0$ were carried out using the following steps. First, we used rejection sampling to simulate a distribution of initial population frequencies (p_0) for a given value of $\hat{p}_0$. For each SNP, we sampled a true population frequency (p_0) from a neutral stationary distribution (*i.e.*, a single draw from a symmetric beta distribution with parameters theta = 0.05, which corresponds to the population-scaled mutation rate for the locus)[89]. We then generated a frequency estimate for the SNP from a single draw from a binomial distribution with parameters p_0 and n_0 = 182, where n_0 is the number of genes sampled in the historic population. We retained the first 10^4 simulated SNPs whose estimate after binomial sampling matched the focal value of $\hat{p}_0$. From the retained SNPs, we carried out forward Wright-Fisher simulations under pure drift for *t* generations to determine the contemporary population frequency (p_t) for each SNP. We then carried out a second round of binomial sampling (with parameters p_t and n_t) for each SNP to generate a final allele frequency estimate. The frequency estimates were used to calculate $\hat{y}_t$ for each simulated SNP. Fig. S18 shows simulated distributions of $\hat{y}_t$ for different values initial frequency estimates ($\hat{p}_0$). The distributions are roughly independent of $\hat{p}_0$ and their 95% CI are well-approximated by the 95% confidence interval predicted by a normal distribution with variance corresponding to our analytical expression for $var[\hat{y}_t]$ (see above).

1314 **REFERENCES**

1315 1. Colautti, R. I., Maron, J. L. & Barrett, S. C. H. Common garden comparisons of native and
1316 introduced plant populations: latitudinal clines can obscure evolutionary inferences. *Evol.*
1317 *Appl.* **2**, 187–199 (2009).
1318 2. Oduor, A. M. O., Leimu, R. & van Kleunen, M. Invasive plant species are locally adapted
1319 just as frequently and at least as strongly as native plant species. *J. Ecol.* **104**, 957–968
1320 (2016).
1321 3. Hodgins, K. A., Bock, D. G. & Rieseberg, L. H. Trait evolution in invasive species. *Annual*
1322 *Plant Reviews Online* 459–496 (2018).
1323 4. Colautti, R. I. & Barrett, S. C. H. Rapid adaptation to climate facilitates range expansion of
1324 an invasive plant. *Science* **342**, 364–366 (2013).
1325 5. Essl, F. *et al.* Biological flora of the British isles:Ambrosia artemisiifolia. *J. Ecol.* **103**, 1069–
1326 1098 (2015).
1327 6. Bagarozzi, D. A., Jr & Travis, J. Ragweed pollen proteolytic enzymes: possible roles in
1328 allergies and asthma. *Phytochemistry* **47**, 593–598 (1998).
1329 7. Schaffner, U. *et al.* Biological weed control to relieve millions from Ambrosia allergies in
1330 Europe. *Nat. Commun.* **11**, 1745 (2020).
1331 8. Lake, I. R. *et al.* Climate Change and Future Pollen Allergy in Europe. *Environ. Health*
1332 *Perspect.* **125**, 385–391 (2017).
1333 9. Ziska, L. *et al.* Recent warming by latitude associated with increased length of ragweed
1334 pollen season in central North America. *Proc. Natl. Acad. Sci. U. S. A.* **108**, 4248–4251
1335 (2011).
1336 10. van Boheemen, L. A. & Hodgins, K. A. Rapid repeatable phenotypic and genomic
1337 adaptation following multiple introductions. *Mol. Ecol.* **29**, 4102–4117 (2020).
1338 11. Bieker, V. C. *et al.* Uncovering the hologenomic basis of an extraordinary plant invasion.

bioRxiv (2022) doi:10.1101/2022.02.03.478494.

12. Chauvel, B., Dessaint, F., Cardinal-Legrand, C. & Bretagnolle, F. The historical spread of Ambrosia artemisiifolia L. in France from herbarium records. *J. Biogeogr.* **33**, 665–673 (2006).
13. van Boheemen, L. A. *et al.* Multiple introductions, admixture and bridgehead invasion characterize the introduction history of Ambrosia artemisiifolia in Europe and Australia. *Mol. Ecol.* **26**, 5421–5434 (2017).
14. van Boheemen, L. A., Atwater, D. Z. & Hodgins, K. A. Rapid and repeated local adaptation to climate in an invasive plant. *New Phytol.* **222**, 614–627 (2019).
15. Seebens, H. *et al.* No saturation in the accumulation of alien species worldwide. *Nat. Commun.* **8**, 14435 (2017).
16. Fisher, R. A. *The Genetical Theory of Natural Selection*. (The Clarendon Press, 1930).
17. Kimura, M. *The Neutral Theory of Molecular Evolution*. (Cambridge University Press, 1983).
18. Orr, H. A. The population genetics of adaptation: The distribution of factors fixed during adaptive evolution. *Evolution* **52**, 935–949 (1998).
19. Yeaman, S. & Whitlock, M. C. The genetic architecture of adaptation under migration-selection balance. *Evolution* **65**, 1897–1911 (2011).
20. Yeaman, S., Gerstein, A. C., Hodgins, K. A. & Whitlock, M. C. Quantifying how constraints limit the diversity of viable routes to adaptation. *PLoS Genet.* **14**, e1007717 (2018).
21. Hermisson, J. & Pennings, P. S. Soft sweeps: molecular population genetics of adaptation from standing genetic variation. *Genetics* **169**, 2335–2352 (2005).
22. Kirkpatrick, M. & Barton, N. Chromosome inversions, local adaptation and speciation. *Genetics* **173**, 419–434 (2006).
23. Wellenreuther, M. & Bernatchez, L. Eco-Evolutionary Genomics of Chromosomal Inversions. *Trends Ecol. Evol.* **33**, 427–440 (2018).
24. Krimbas, C. B. & Powell, J. R. *Drosophila Inversion Polymorphism*. (CRC Press, 1992).

1365 25. Lowry, D. B. & Willis, J. H. A widespread chromosomal inversion polymorphism contributes
1366 to a major life-history transition, local adaptation, and reproductive isolation. *PLoS Biol.* **8**,
1367 (2010).
1368 26. Todesco, M. *et al.* Massive haplotypes underlie ecotypic differentiation in sunflowers.
1369 *Nature* **584**, 602–607 (2020).
1370 27. Kirkpatrick, M. & Barrett, B. Chromosome inversions, adaptive cassettes and the evolution
1371 of species' ranges. *Mol. Ecol.* **24**, 2046–2055 (2015).
1372 28. Putnam, N. H. *et al.* Chromosome-scale shotgun assembly using an in vitro method for
1373 long-range linkage. *Genome Res.* **26**, 342–350 (2016).
1374 29. Kubešová, M. *et al.* Naturalized plants have smaller genomes than their non-invading
1375 relatives: a flow cytometric analysis of the Czech alien flora. *Preslia* **82**, 81–96 (2010).
1376 30. Bai, C., Alverson, W. S., Follansbee, A. & Waller, D. M. New reports of nuclear DNA
1377 content for 407 vascular plant taxa from the United States. *Ann. Bot.* **110**, 1623–1629
1378 (2012).
1379 31. Manni, M., Berkeley, M. R., Seppey, M., Simão, F. A. & Zdobnov, E. M. BUSCO Update:
1380 Novel and Streamlined Workflows along with Broader and Deeper Phylogenetic Coverage
1381 for Scoring of Eukaryotic, Prokaryotic, and Viral Genomes. *Mol. Biol. Evol.* **38**, 4647–4654
1382 (2021).
1383 32. Barker, M. S. *et al.* Multiple paleopolyploidizations during the evolution of the Compositae
1384 reveal parallel patterns of duplicate gene retention after millions of years. *Mol. Biol. Evol.*
1385 **25**, 2445–2455 (2008).
1386 33. Badouin, H. *et al.* The sunflower genome provides insights into oil metabolism, flowering
1387 and Asterid evolution. *Nature* **546**, 148–152 (2017).
1388 34. Holt, C. & Yandell, M. MAKER2: an annotation pipeline and genome-database
1389 management tool for second-generation genome projects. *BMC Bioinformatics* **12**, 491
1390 (2011).

1391 35. Zagotta, M. T. *et al.* The Arabidopsis ELF3 gene regulates vegetative photomorphogenesis
1392 and the photoperiodic induction of flowering. *Plant J.* **10**, 691–702 (1996).
1393 36. Martin, A. & Orgogozo, V. The Loci of repeated evolution: a catalog of genetic hotspots of
1394 phenotypic variation. *Evolution* **67**, 1235–1250 (2013).
1395 37. Gautier, M. Genome-Wide Scan for Adaptive Divergence and Association with Population-
1396 Specific Covariates. *Genetics* **201**, 1555–1579 (2015).
1397 38. Fick, S. E. & Hijmans, R. J. WorldClim 2: new 1-km spatial resolution climate surfaces for
1398 global land areas. *Int. J. Climatol.* **37**, 4302–4315 (2017).
1399 39. Booker, T. R., Yeaman, S. & Whitlock, M. C. The WZA: A window-based method for
1400 characterizing genotype-environment association. *bioRxiv* 2021.06.25.449972 (2021)
1401 doi:10.1101/2021.06.25.449972.
1402 40. Prapas, D. *et al.* QTL analysis reveals an oligogenic architecture of a rapidly adapting trait
1403 during the European invasion of common ragweed. *bioRxiv* (2022)
1404 doi:10.1101/2022.02.24.481758.
1405 41. Werck-Reichhart, D., Bak, S. & Paquette, S. Cytochromes p450. *Arabidopsis Book* **1**,
1406 e0028 (2002).
1407 42. Gupta, R. & Chakrabarty, S. K. Gibberellic acid in plant: still a mystery unresolved. *Plant*
1408 *Signal. Behav.* **8**, (2013).
1409 43. Li, H. & Ralph, P. Local PCA Shows How the Effect of Population Structure Differs Along
1410 the Genome. *Genetics* **211**, 289–304 (2019).
1411 44. Haldane, J. B. S. The theory of a cline. *J. Genet.* **48**, 277–284 (1948).
1412 45. Thurman, T. J. & Barrett, R. D. H. The genetic consequences of selection in natural
1413 populations. *Mol. Ecol.* **25**, 1429–1448 (2016).
1414 46. Chen, K.-W., Marusciac, L., Tamas, P. T., Valenta, R. & Panaitescu, C. Ragweed Pollen
1415 Allergy: Burden, Characteristics, and Management of an Imported Allergen Source in
1416 Europe. *Int. Arch. Allergy Immunol.* **176**, 163–180 (2018).

1417 47. Stern, D. L. The genetic causes of convergent evolution. *Nat. Rev. Genet.* **14**, 751–764
1418 (2013).
1419 48. Sun, Y. *et al.* Climate warming can reduce biocontrol efficacy and promote plant invasion
1420 due to both genetic and transient metabolomic changes. *Ecol. Lett.* **25**, 1387–1400 (2022).
1421 49. Cheng, H., Concepcion, G. T., Feng, X., Zhang, H. & Li, H. Haplotype-resolved de novo
1422 assembly using phased assembly graphs with hifiasm. *Nat. Methods* **18**, 170–175 (2021).
1423 50. Li, H. Aligning sequence reads, clone sequences and assembly contigs with BWA-MEM.
1424 *arXiv [q-bio.GN]* (2013).
1425 51. Sayers, E. W. *et al.* Database resources of the National Center for Biotechnology
1426 Information. *Nucleic Acids Res.* **49**, D10–D17 (2021).
1427 52. Marçais, G. & Kingsford, C. A fast, lock-free approach for efficient parallel counting of
1428 occurrences of k-mers. *Bioinformatics* **27**, 764–770 (2011).
1429 53. Schubert, M., Lindgreen, S. & Orlando, L. AdapterRemoval v2: rapid adapter trimming,
1430 identification, and read merging. *BMC Res. Notes* **9**, 88 (2016).
1431 54. Schubert, M. *et al.* Characterization of ancient and modern genomes by SNP detection and
1432 phylogenomic and metagenomic analysis using PALEOMIX. *Nat. Protoc.* **9**, 1056–1082
1433 (2014).
1434 55. Van der Auwera, G. A. & O'Connor, B. D. *Genomics in the Cloud: Using Docker, GATK,*
1435 *and WDL in Terra*. ('O'Reilly Media, Inc.', 2020).
1436 56. DePristo, M. A. *et al.* A framework for variation discovery and genotyping using next-
1437 generation DNA sequencing data. *Nat. Genet.* **43**, 491–498 (2011).
1438 57. Danecek, P. *et al.* The variant call format and VCFtools. *Bioinformatics* **27**, 2156–2158
1439 (2011).
1440 58. Browning, B. L., Zhou, Y. & Browning, S. R. A One-Penny Imputed Genome from Next-
1441 Generation Reference Panels. *The American Journal of Human Genetics* vol. 103 338–348
1442 Preprint at https://doi.org/10.1016/j.ajhg.2018.07.015 (2018).

1443 59. Flynn, J. M. *et al.* RepeatModeler2 for automated genomic discovery of transposable
1444 element families. *Proc. Natl. Acad. Sci. U. S. A.* **117**, 9451–9457 (2020).
1445 60. Campbell, M. S. *et al.* MAKER-P: a tool kit for the rapid creation, management, and quality
1446 control of plant genome annotations. *Plant Physiol.* **164**, 513–524 (2014).
1447 61. Smit, A. F. A., Hubley, R. & Green, P. RepeatMasker Open-4.0. 2013--2015. Preprint at
1448 (2015).
1449 62. Cantarel, B. L. *et al.* MAKER: an easy-to-use annotation pipeline designed for emerging
1450 model organism genomes. *Genome Res.* **18**, 188–196 (2008).
1451 63. Korf, I. Gene finding in novel genomes. *BMC Bioinformatics* **5**, 59 (2004).
1452 64. Stanke, M., Schöffmann, O., Morgenstern, B. & Waack, S. Gene prediction in eukaryotes
1453 with a generalized hidden Markov model that uses hints from external sources. *BMC*
1454 *Bioinformatics* **7**, 62 (2006).
1455 65. Seppey, M., Manni, M. & Zdobnov, E. M. BUSCO: Assessing Genome Assembly and
1456 Annotation Completeness. *Methods Mol. Biol.* **1962**, 227–245 (2019).
1457 66. Card DC. Genestats.
1458 67. Berardini, T. Z. *et al.* The arabidopsis information resource: Making and mining the 'gold
1459 standard' annotated reference plant genome. *genesis* vol. 53 474–485 Preprint at
1460 https://doi.org/10.1002/dvg.22877 (2015).
1461 68. Camacho, C. *et al.* BLAST+: architecture and applications. *BMC Bioinformatics* **10**, 421
1462 (2009).
1463 69. Alexa, A. & Rahnenführer, J. Gene set enrichment analysis with topGO. *Bioconductor*
1464 *Improv* **27**, 1–26 (2009).
1465 70. Bouché, F., Lobet, G., Tocquin, P. & Périlleux, C. FLOR-ID: an interactive database of
1466 flowering-time gene networks in Arabidopsis thaliana. *Nucleic Acids Res.* **44**, D1167–71
1467 (2016).
1468 71. Cingolani, P. *et al.* A program for annotating and predicting the effects of single nucleotide

polymorphisms, SnpEff: SNPs in the genome of Drosophila melanogaster strain w1118; iso-2; iso-3. *Fly* **6**, 80–92 (2012).

72. Chang, C. C. *et al.* Second-generation PLINK: rising to the challenge of larger and richer datasets. *GigaScience* vol. 4 Preprint at https://doi.org/10.1186/s13742-015-0047-8 (2015).
73. Hijmans, R. J. *et al.* Package 'raster'. *R package* **734**, (2015).
74. Team, R. C. & Others. R: A language and environment for statistical computing. (2013).
75. Kang, H. M. *et al.* Variance component model to account for sample structure in genome-wide association studies. *Nat. Genet.* **42**, 348–354 (2010).
76. Fox, J. *et al.* The car package. *R Foundation for Statistical Computing* **1109**, (2007).
77. Korneliussen, T. S., Albrechtsen, A. & Nielsen, R. ANGSD: Analysis of Next Generation Sequencing Data. *BMC Bioinformatics* **15**, 356 (2014).
78. Meisner, J. & Albrechtsen, A. Inferring Population Structure and Admixture Proportions in Low-Depth NGS Data. *Genetics* **210**, 719–731 (2018).
79. Lenth, R., Singmann, H., Love, J., Buerkner, P. & Herve, M. Package 'emmeans'. Preprint at https://cran.microsoft.com/snapshot/2018-01-13/web/packages/emmeans/emmeans.pdf (2019).
80. Rastas, P., Paulin, L., Hanski, I., Lehtonen, R. & Auvinen, P. Lep-MAP: fast and accurate linkage map construction for large SNP datasets. *Bioinformatics* **29**, 3128–3134 (2013).
81. Otto, S. P. & Day, T. *A Biologist's Guide to Mathematical Modeling in Ecology and Evolution*. (Princeton University Press, 2011).
82. Hartl, D. L. & Clark, A. G. *Principles of Population Genetics*. (Sinauer, 2007).
83. Connallon, T. & Clark, A. G. Antagonistic versus nonantagonistic models of balancing selection: characterizing the relative timescales and hitchhiking effects of partial selective sweeps. *Evolution* **67**, 908–917 (2013).
84. Chevin, L., Gompert, Z. & Nosil, P. Frequency dependence and the predictability of evolution in a changing environment. *Evolution Letters* vol. 6 21–33 Preprint at

https://doi.org/10.1002/evl3.266 (2022).

85. Crow, J. F. & Kimura, M. *An Introduction to Population Genetics Theory*. vol. 26 977 (The Blackburn Press, 1971).

86. Felsenstein, J. *Theoretical Evolutionary Genetics*. (2019).

87. Roughgarden, J. *Theory of population genetics and evolutionary ecology: an introduction*. (sidalc.net, 1979).

88. Lasne, C., Sgrò, C. M. & Connallon, T. The Relative Contributions of the X Chromosome and Autosomes to Local Adaptation. *Genetics* **205**, 1285–1304 (2017).

89. Wright, S. Evolution in Mendelian Populations. *Genetics* **16**, 97–159 (1931).